Lattice instability and enhancement of superconductivity in YB_6

N. Sluchanko,* V. Glushkov, and S. Demishev
Prokhorov General Physics Institute of RAS, 38 Vavilov Street, 119991 Moscow, Russia
and Moscow Institute of Physics and Technology, 9 Institutskiy Lane, 141700 Dolgoprudny, Moscow Region, Russia

A. Azarevich, M. Anisimov, A. Bogach, and V. Voronov
Prokhorov General Physics Institute of RAS, 38 Vavilov Street, 119991 Moscow, Russia

S. Gavrilkin and K. Mitsen
Lebedev Physical Institute of RAS, 53 Leninskiy Avenue, 119991 Moscow, Russia

A. Kuznetsov and I. Sannikov
National Research Nuclear University MEPhI, 31 Kashirskoe Shosse, 115409 Moscow, Russia

N. Shitsevalova and V. Filipov
Frantsevich Institute for Problems of Materials Science of NASU, 3 Krzhyzhanovsky Street, 03680 Kiev, Ukraine

M. Kondrin
Vereshchagin Institute for High Pressure Physics of RAS, 14 Kaluzhskoe Shosse, 142190 Troitsk, Russia

S. Gabáni and K. Flachbart
Institute of Experimental Physics of SAS, 47 Watsonova Street, SK-04001 Košice, Slovak Republic
(Received 31 August 2016; revised manuscript received 1 December 2016; published 3 October 2017)

The superconducting and normal state characteristics of yttrium hexaboride (YB_6) have been investigated for the single crystals with a transition temperatures T_c ranging between 4.2 K and 7.6 K. The extracted set of microscopic parameters [the coherence length $\xi(0) \sim 320$–340 Å, the penetration depth $\lambda(0) \sim 1100$–3250 Å and the mean free path of charge carriers $l = 11$–58 Å, the Ginzburg-Landau-Maki parameters $\kappa_{1,2}(0) \sim 3.3$–9.5, and the superconducting gap $\Delta(0) \sim 6.2$–14.8 K] confirms the type II superconductivity in "dirty limit" ($\xi \gg l$) with a medium to strong electron-phonon interaction (the electron-phonon interaction constant $\lambda_{e\text{-}ph} = 0.32$–$0.96$) and s-type pairing of charge carriers in this compound [$2\Delta(0)/k_B T_c \approx 3$–$4$]. The comparative analysis of charge transport (resistivity, Hall and Seebeck coefficients) and thermodynamic (heat capacity, magnetization) properties in the normal state in YB_6 allowed to assume a transition into the cage-glass state at $T^* \sim 50$ K with a static disorder in the arrangement of the Y^{3+} ions. We argue that the significant T_c variations in YB_6 single crystals are determined by two main factors: (i) the superconductivity enhancement is related with the increase of the number of vacancies, both at yttrium and boron sites, leading to nonstoichiometric composition, which is accompanied by the enhancement of electron-phonon interaction in the hexaboride lattice; (ii) stronger T_c depression is observed in near stoichiometric and more dense crystals and it is induced by the development of *bcc* lattice instability producing strong distortion, disordering, and formation of defect complexes in the matrix of YB_6.

DOI: 10.1103/PhysRevB.96.144501

I. INTRODUCTION

The discovery of high-temperature superconductivity in magnesium diboride (MgB_2) with $T_c \sim 39$ K [1] stimulated an interest in the study of microscopic mechanisms, which are responsible for superconductivity in higher borides RB_6 and RB_{12} with a rigid covalent framework composed of boron clusters. The maximum transition temperature in these model superconductors-cage glasses [2] was observed in yttrium hexaboride YB_6 ($T_c \sim 8$ K [3]) in which the pairing is mainly influenced by low-energy (~8 meV) Einstein-like quasilocal vibrations of yttrium ions bound loosely in the B_{24} cuboctahedra of the boron sublattice.

The strong T_c dispersion (1.5–8.4 K) reported for YB_6 samples by different authors [3–8] has no satisfactory explanation up to now. For example, the YB_6 single crystals grown by a modified Al-Ga flux growth method in Al_2O_3 crucible under Ar pressure show $T_c = 5.8 \pm 0.1$ K regardless on the initial composition. The T_c values for samples grown by argon arc melting are 6.8–7.0 K. For YB_6 with nominal compositions obtained by ultrafast quenching from melt the starting point of the resistive transition to superconducting state was observed at $T_c \sim 8.4$ K [4]. Superconducting transition temperatures of YB_6 single crystals grown by induction zone melting also reach high values $T_c = 7.2$ K [3], 7.5 K [5,6], and 7.7 K [7]. The lowest values of $T_c = 1.5$–6.3 K were reported for powder samples prepared by the borothermal reduction [8]. To explain such a significant T_c variation it was suggested in Ref. [3] that the transition temperature is controlled by the B/Y ratio (the highest T_c was obtained

*Corresponding author: nes@lt.gpi.ru

 ©2017 American Physical Society

for a B/Y < 6). Thus, both a growth of a number of boron vacancies, which is associated with the deviation from the stoichiometric composition of the boron sublattice, and a decrease of yttrium vacancies in contrast, which requires a stoichiometric metal sublattice composition, result according to Ref. [3] in a T_c enhancement in this compound. However, this conclusion contradicts clearly observations made in Ref. [6] where the highest T_c was observed on the sample with the lowest residual resistivity. Moreover, whereas the microanalysis results [3] indicate a significant concentration of boron vacancies (for $YB_{5.7–5.8}$ composition), the most of the YB_6 single crystals grown by zone melting [9] correspond approximately to a composition $YB_{6.1}$, which points to the presence of yttrium vacancies in the hexaboride matrix. It should be emphasized that some of the mentioned methods of YB_6 synthesis correspond to nonequilibrium crystallization conditions. This fact allows us to assume that the superconducting transition temperature can be significantly modified in the nonequilibrium, metastable state of yttrium hexaboride. A fairly large residual resistivity $\rho_0 \sim 8–25\ \mu\Omega$ cm and a rather small residual resistivity ratio $\rho(300\ \mathrm{K})/\rho_0 = 2–4.5$ observed for all the YB_6 single crystals studied up to now also indicate strong low temperature scattering of charge carriers on crystal structure defects and inhomogeneities, which can be associated also with a nonequilibrium state of yttrium hexaboride.

According to the conclusion of Ref. [10] YB_6 is located on the border of stability of the RB_6 structure corresponding to the smallest size of metallic (Y^{3+}) ion in the hexaboride family and, hence, being unstable with respect to decomposition into neighboring binary phases. Similarly to other higher borides, the YB_6 crystal lattice is stabilized in the homogeneity range by introducing structural defects, predominantly vacancies in the metal and boron sublattices [11,12]. As a result, YB_6 strongly differs, for example, from LaB_6. Actually, the electrical resistivity of YB_6 is five-eight times larger than that of LaB_6 at room temperature (see Fig. 2 below), the mass M_R ratio of yttrium and lanthanum ions is 0.64, and the ratio of phonon frequencies ω_R of these two ions is about 0.62. This points to a large amplitude of Y vibrations given by $(\hbar/2M_R\omega_R)^{1/2}$ and thus to a strong electron-phonon coupling, which is, roughly speaking, proportional to the amplitude of the *R*—ion's quasilocal vibrations. The strong phonon softening in YB_6 (8 meV) in comparison with LaB_6 (13 meV) may therefore be attributed to the decreasing potential of yttrium quasistable sites [13].

Superconducting T_c enhancement in the vicinity of lattice instabilities in the nonequilibrium state is a well-known effect which is up to now not well understood in detail. For example, the amorphous beryllium films deposited by evaporation on low temperature substrates show T_c of about 10 K enhanced if compared with $T_c = 0.026$ K for the *hcp* phase of Be [14,15]. The value of T_c in Ga thin films prepared by condensation at low temperatures increases up to 8.4 K from that of 1.1 K for bulk gallium [16]. Nonequilibrium $Al_{1-x}Si_x$ solid solutions demonstrate a T_c variation between 1.18 K ($x = 0$) and 11 K ($x \sim 0.2$), their superconductivity enhancement being attributed to a lattice instability developed in these *fcc* Al-based crystals [17–20]. Therefore, it is interesting to consider YB_6 crystals with different T_c values from the point of view of nonequilibrium superconductivity investigating correlation between *bcc* lattice instability and T_c changes.

In this context the presented results of detailed studies of specific heat, magnetization, resistivity, Hall and Seebeck coefficients, and hydrostatic density in YB_6 single crystals with different values of T_c in the range between 4.2 K and 7.6 K allowed us to elucidate the mechanism, which is responsible for the enhancement/suppression of superconductivity. We argue that development of lattice instability occurs in the stoichiometric YB_6 located on the border of stability of RB_6 row. The instability overcomes in the presence of isolated vacancies on boron and yttrium sites of the boride matrix, and it is the main factor which controls the observed T_c changes.

The paper is organized as follows: Experimental details and results are shown in Secs. II and III, respectively. In the discussion part IV A the data analysis of the superconducting state is presented and we argue in favor of type II superconductivity in the "dirty limit" with a medium to strong electron-phonon interaction and *s*-type pairing of charge carriers in YB_6. In part IV B a detailed analysis of the normal state parameters is undertaken which allowed us to assume that below $T^* \sim 50$ K a cage-glass state forms in YB_6. Final conclusions are formulated in Sec. V.

II. EXPERIMENTAL DETAILS

Measurements were performed on four single crystals of yttrium hexaboride with $T_c = 4.2$ K (No. 4), 6.2 K (No. 3), 7.3 K (No. 2), and 7.4 K (No. 1) (according to results of zero-field heat capacity measurements). It is argued below (see Sec. IV B and Fig. 14) that the main difference between YB_6 single crystals No. 1–No. 4 is caused by the number of vacancies producing mass density changes in the samples. Thus, the higher T_c crystals No. 1 and No. 2 are characterized by the nonstoichiometric composition with a high number of Y and B vacancies in the hexaboride matrix. On the contrary, the dense and near stoichiometric YB_6 samples No. 3 and No. 4 are nonequilibrium, distorted crystals with lower T_c values. The studied single crystals were grown by induction zone melting in IPM NASU, Kiev, using rods sintered from powder obtained by borothermal reduction of yttrium oxide (Y_2O_3) with a purity of 99.999% and amorphous boron having a purity of >99.5%. Taking into account the nature of the peritectic melting of YB_6, we synthesized the initial powder with boron excess. Crystal growth from the boron enriched melt allowed us to (i) decrease the melting temperature below the peritectic one (2600 °C) [10], (ii) obtain single-phase ingots, and (iii) improve the real structure of crystals. The optimum boron composition of the initial sintered rods was consistent with $YB_{6.65}$–$YB_{6.85}$. Other optimization parameters were the pressure of high purity argon gas in the growth chamber (0.7 MPa) and the crystallization rate (0.22 mm/min). Because of the zone cleaning effect during the process of crystal growth the impurity concentration did not exceed 0.001 wt.%. In order to control the composition of samples we used additional optical emission spectral and microanalysis techniques. The quality and single phase of crystals were controlled by x-ray methods. As an example, Fig. 1 shows the diffraction pattern of a polished plate cut perpendicularly to the growth axis [panel (a)] and the Laue backscattering patterns [panels (b) and (c)]

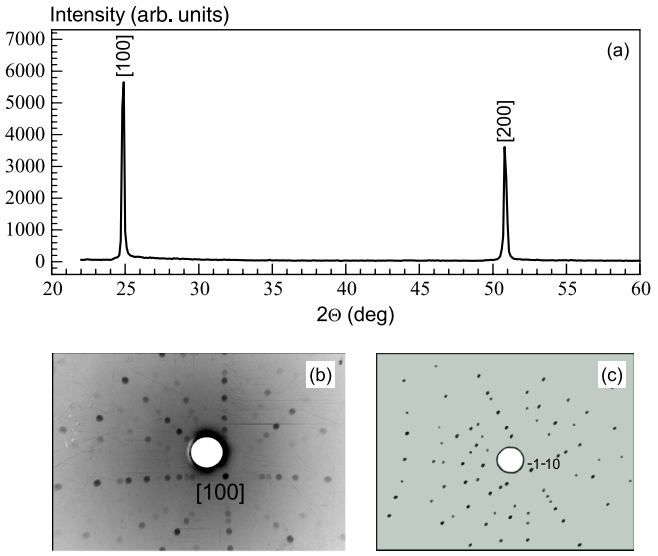

FIG. 1. X-ray diffraction pattern of a polished plate cut perpendicular to the growth axis obtained in Co K_α radiation with an Fe filter [panel (a)] and Laue backscattering patterns [panels (b) and (c)] in Co K_a radiation for crystals YB_6 No. 2 ($T_c = 7.3$ K) and No. 4 ($T_c = 4.2$ K), correspondingly. In the last case the deviation of the growth direction from $[\bar{1}\bar{1}0]$ axis was about 7°.

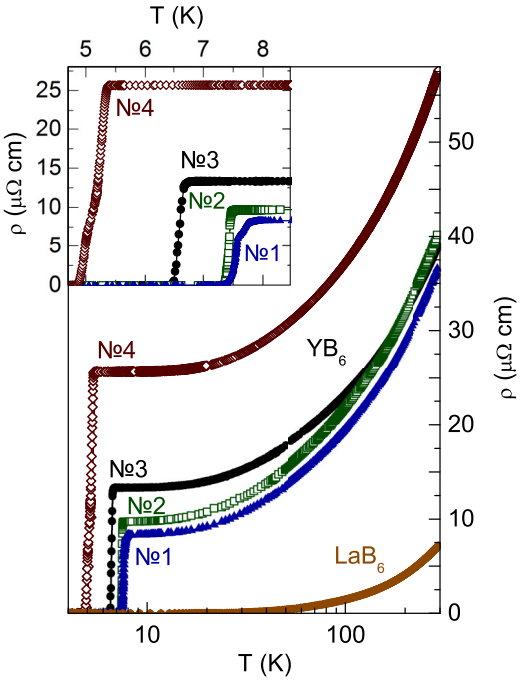

FIG. 2. Temperature dependences of resistivity $\rho(T)$ for different YB_6 samples. The $\rho(T)$ curve of the LaB_6 crystal is also shown for comparison. Inset shows the region of the superconducting transition.

of YB_6 crystals No. 2 ($T_c = 7.3$ K) and No. 4 ($T_c = 4.2$ K), correspondingly. In the last case the deviation of the growth direction from $[\bar{1}\bar{1}0]$ axis was about 7°. The obtained value of the lattice constant $a = 4.1001 \pm 0.0005$ Å is identical within the experimental accuracy for all four investigated single crystals. The heat capacity and Hall effect were measured using a Quantum Design installation PPMS-9 in the Shared Facility Centre of Lebedev Physical Institute of RAS in the temperature range 1.9–300 K and in magnetic fields up to 9 T. For crystals No. 3 and No. 4 additional heat capacity studies have been carried out at temperatures in the interval 0.4–2 K. Field and temperature dependences of magnetization were recorded both by a Quantum Design MPMS-5 and a SQUID magnetometer [21]. For measurements of resistivity and thermoelectric power we used the original setup described in Refs. [22,23], respectively. The technique applied for the measurement of hydrostatic density of samples is described in detail in Ref. [24].

III. RESULTS AND DISCUSSION

A. Resistivity

Figure 2 shows the temperature dependences of resistivity $\rho(T)$ of all four studied YB_6 crystals. The $\rho(T)$ curve of the LaB_6 crystal is also shown for comparison. The $\rho(T)$ curves exhibit a typical metallic behavior with a rather small residual resistivity ratio $\rho(300\ \mathrm{K})/\rho_0 = 2.2$–$4.5$ for YB_6. The residual resistivity $\rho_0 \approx 8\,\mu\Omega$ cm of sample No. 1 with the highest $T_c = 7.55$ K is the smallest among YB_6 crystals, but it is about 470 times higher than that of LaB_6. The increase of ρ_0 is accompanied by a decrease of T_c [Fig. 2] which is in accordance with results of Refs. [3] and [6]. Inset in Fig. 2 shows the $\rho(T)$ dependence in the vicinity of the superconducting transition. For all YB_6 single crystals studied we observed a wide enough resistivity transition with a width of $\Delta T_c^{(\rho)} \sim 0.12$–$0.45$ K [Table I] as well as nonmonotonous $\rho(T)$ behavior near T_c, which is a particularly discerned for sample No. 1 with maximal T_c. The $T_c^{(\rho)}$ values found as midpoints $\rho(T_c) = 1/2\rho_0$ of resistivity transitions are shown in Table I.

TABLE I. Superconducting state parameters obtained from heat capacity measurements: $T_c^{(C)}$ and $\Delta T_c^{(C)}$ are the transition temperature and the width of transition, H_{cm} and H_{c2} the thermodynamic and the second critical fields, ΔC the heat capacity jump at T_c, $\Delta(0)$ the superconducting gap, $\kappa_1(0)$ the Ginzburg-Landau-Maki parameter, $\xi(0)$ the coherence length, and $\lambda(0)$ the penetration depth. Also shown are the transition temperature $T_c^{(\rho)}$ and the width of the transition $\Delta T_c^{(\rho)}$, obtained from resistivity measurements.

	No. 1	No. 2	No. 3	No. 4
$T_c^{(\rho)}/T_c^{(C)}$ (K)	7.55/7.38	7.4/7.3	6.6/6.2	5.2/4.2
$\Delta T_c^{(\rho)}/\Delta T_c^{(C)}$ (K)	0.3/0.15	0.12/0.15	0.2/0.4	0.45/0.5
H_{cm} (Oe)	618	613	429	211.2
ΔC (mJ/mol K)	62.1	59	29.3	15.1
$\Delta C/\gamma T_c$	2.21	2.1	1.24	1.39
$\Delta(0)$ (K)	14.8	14.6	12.1	6.2
$2\Delta(0)/T_c$	4.01	3.99	3.91	2.95
$H_{c2}(0)$ (Oe)	2850	2912	2927	2840
dH_{c2}/dT (Oe/K)	–559	–575	–623	–980
$\kappa_1(0)$	3.26	3.36	4.82	9.5
$\xi(0)$ (Å)	340	336.4	335.5	340.6
$\lambda(0)$ (Å)	1109	1130	1618	3242

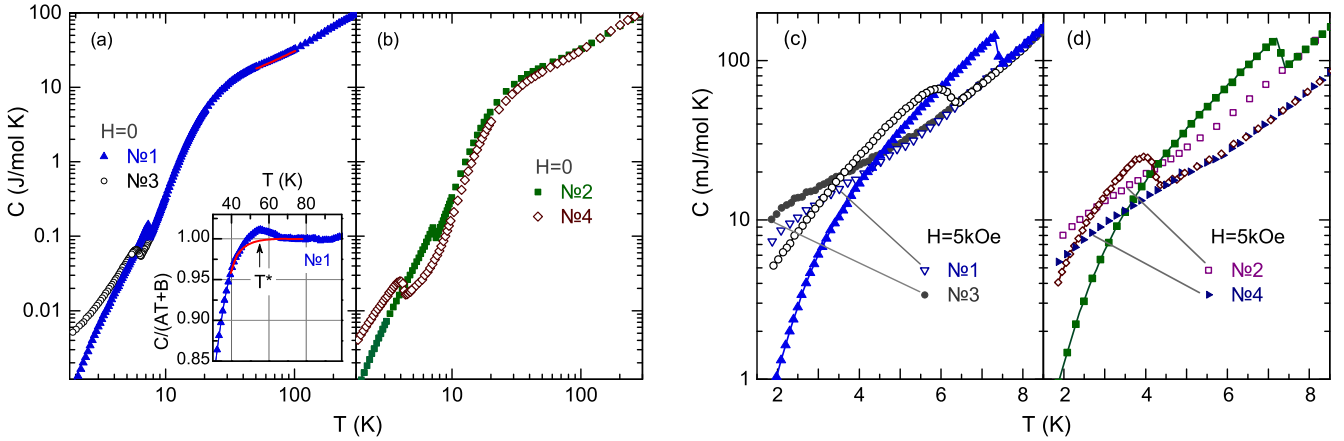

FIG. 3. (a), (b) Temperature dependences of the heat capacity for different YB_6 samples measured in zero magnetic field. Panels (c) and (d) show an enlarged area around the transition temperature; data at $H = 5$ kOe correspond to the normal state of YB_6. The inset on panel (a) shows the fragment of experimental curve in coordinates $C(T)/(AT + B)$ vs T for sample No. 1 (see text).

B. Specific heat

The heat capacity temperature dependences $C(T)$ of the investigated YB_6 single crystals are shown in Fig. 3. Panels (c) and (d) in Fig. 3 highlight the heat capacity behavior in the vicinity of the superconducting phase transition. In addition, Fig. 3 shows also the $C(T)$ curves measured in the magnetic field of 5 kOe in which the superconductivity of yttrium hexaboride is completely suppressed. As can be seen in Fig. 3, a gradual diminution of the heat capacity at temperatures between 300 K and 50 K is followed by a sharp almost steplike decrease with a typical Einstein-type $C(T)$ dependence below 40 K. It is worth noting that although in the normal state at $T > 30$ K the $C(T)$ curves of all four YB_6 samples are almost identical in the double logarithmic plot used in Fig. 3, the position of the steplike $C(T)$ anomaly of crystal No. 4 shifts up along the T axis when compared with other YB_6 samples. Then, at temperatures between 140 K and 300 K the heat capacity of crystal No. 4 becomes the highest (see also Fig. 17).

The results of specific heat measurements at low temperatures and in small magnetic fields which just destroy superconductivity are presented in Fig. 4. For comparison, heat capacity curves are shown in this figure for samples No. 1, No. 3, and No. 4 with a significantly different T_c [see panels (a), (b), and (c), respectively] in coordinates $C(T, H_0)/T$ vs T. Apart from T_c changes between samples No. 1, No. 2, No. 3, and No. 4 there are also differences related with both lowering of the jump amplitude ΔC near T_c and with the broadening of this anomaly [see panels (b) and (c) in Fig. 4 and Table I]. Figures 5(a) and 5(b) show the low-temperature heat capacity of samples No. 2, No. 3, and No. 4 in coordinates $C(T, H_0)/T$ vs T^2, which is commonly used to determine the Sommerfeld coefficient γ of the electronic heat capacity. For YB_6 crystals No. 1 and No. 2 the obtained values $\gamma \approx 3.8$–3.85 mJ/(mol K^2) coincide with each other, whereas the low temperature specific heat of samples No. 3 and No. 4 is obviously influenced by a moderate additional magnetic contribution. It should be mentioned here that magnetic defects, clusters, and spin glass behavior can result into a specific heat enhancement [25] and lead in some cases also to a false indication of heavy fermion behavior [26,27]. In such cases a detailed investigation of magnetic field changes of the low temperature heat capacity can help to identify the nature of the enhancement. For this reason we have carried out

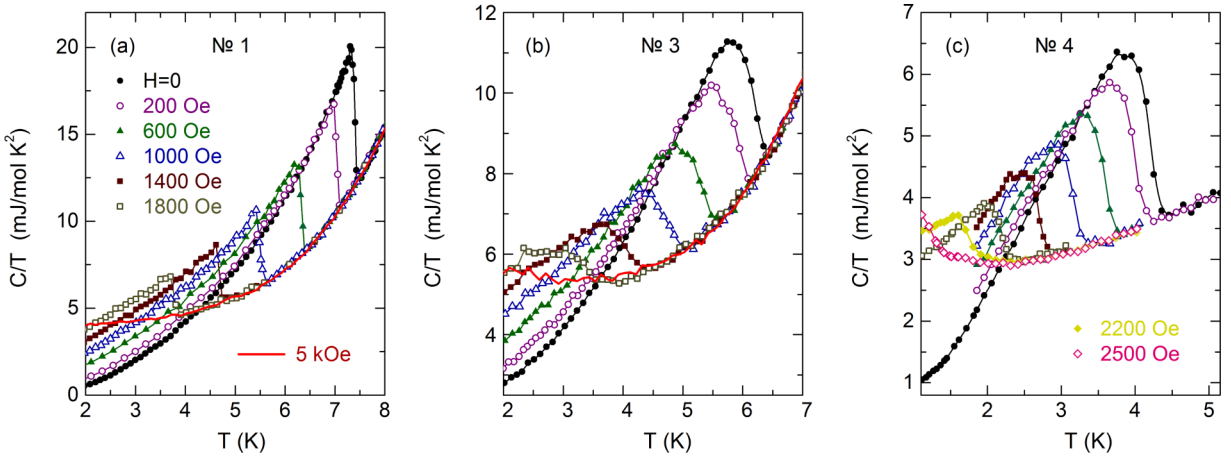

FIG. 4. Dependences of the low temperature heat capacity $C/T = f(T)$ of YB_6 samples (a) No. 1, (b) No. 3, and (c) No. 4 measured in different external magnetic fields $H \leqslant 5$ kOe.

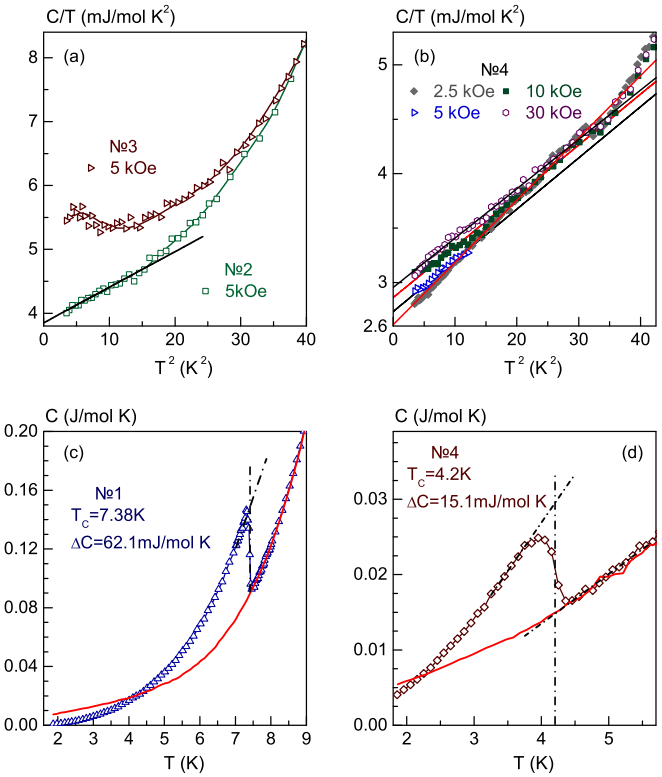

FIG. 5. (a) Dependences of the low temperature heat capacity of YB_6 in the coordinates C/T vs T^2 for samples No. 2, No. 3 [panel (a)], and No. 4 [panel (b)] for different values of external magnetic field $H \leqslant 30$ kOe. Panels (c) and (d) show the procedure applied to determine the ΔC jump amplitude near T_c in samples No. 1 and No. 4.

field dependent heat capacity measurements on crystals No. 3 and No. 4 at temperatures 0.4–7 K and in magnetic fields $H \geqslant 2.5$ kOe. The obtained magnetic component prevails essentially the electronic Sommerfeld term and demonstrates a moderate increase in external magnetic field [for No. 3 see, for example Fig. 6(a)]. The magnetic anomaly shifts up along the temperature axis when the magnetic field increases (see Fig. 6). Thus, the results obtained for crystal No. 3 do not enable us to estimate properly the value of the electronic contribution without the separation of low temperature heat capacity components. The detailed data analysis is presented below and in Ref. [28] (see Fig. S1). On the contrary, for crystal No. 4 the magnetic contribution is small enough and we estimate $\gamma \approx 2.59$ mJ/(mol K^2) directly from the extrapolation of the $C/T = f(T^2, H = 2.5\,\text{kOe})$ dependence to zero temperature [Fig. 5(b)].

In Figs. 5(c) and 5(d) the determination procedure of the transition temperature T_c and of the heat capacity jump at T_c are shown for samples No. 1 and No. 4, correspondingly. The magnitude of the jump ΔC was determined as the length of the vertical line between the asymptotics of temperature dependences of the specific heat in the normal and superconducting states [see Figs. 5(c) and 5(d)]. The obtained ΔC values are presented in Table I. Note that the superconducting transition temperatures deduced from heat capacity measurements are similar ($\Delta T_c \sim 0.15$–0.5 K) to

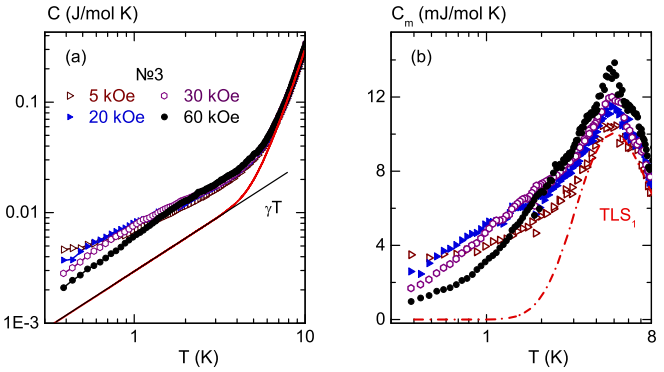

FIG. 6. (a) Heat capacity dependences of sample No. 3 at temperatures 0.4–10 K in external magnetic field $H \leqslant 60$ kOe. The black linear γT dependence corresponds to the Sommerfeld term with $\gamma \approx 2.94$ mJ/(mol K^2). The red solid line shows the experimental curve approximation by sum $\gamma T + C_D + C_E + C_{\text{Sh}_2}$ [see text and Eqs. (14)–(16) for details]. Panel (b) shows the magnetic component $C_m = C - \gamma T - C_D - C_E - C_{\text{Sh}_2}$ of sample No. 3. TLS_1 (dash-dot line) indicates the Shottky component C_{Sh_1} [see Eq. (16)] of the heat capacity (the detailed analysis is presented in Ref. [28]).

those obtained both from resistivity [Fig. 2] and field-cooled ($H \sim$ 4–8 Oe) magnetization curves (see inset in Fig. 7 and Tables I and II for the comparison of T_c values). To minimize the errors of T_c evaluation a special calibration procedure of the temperature sensors used in PPMS-9 (Quantum Design) and in the installation for resistivity measurements [14] was carried out. The obtained differences between the T_c data from resistivity [$T_c^{(\rho)}$] and heat capacity measurements [$T_c^{(C)}$] are therefore probably caused due to the presence of very small number of phases with high T_c values, which within the

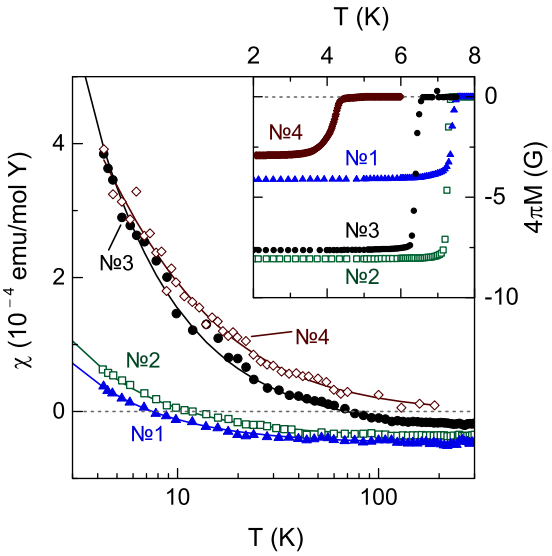

FIG. 7. Temperature dependences of the magnetic susceptibility $\chi(T) = M(T)/H$ for different samples of YB_6, measured in the magnetic field of 5.4 kOe. Solid lines show the fitting of experimental data by Eq. (17). The inset shows the superconducting transition measured during cooling at $H = 4$ Oe (No. 1), 8 Oe (No. 2), 7.5 Oe (No. 3), and 3 Oe (No. 4).

TABLE II. Parameters of the superconducting state obtained from magnetization measurements: T_c and ΔT_c denote the transition temperature and the width of the transition, H_{cm}, H_{c1}, and H_{c2} the thermodynamic, the first and the second critical fields, $\kappa_2(0)$ the Ginzburg-Landau-Maki parameter, $\xi(0)$ the coherence length, $\lambda(0)$ the penetration depth, and a the parameter of relation (10).

	No. 1	No. 2	No. 3	No. 4
T_c (K)	7.55	7.4	6.6	4.2
ΔT_c (K)	0.25	0.15	0.35	0.4
H_{cm} (Oe)	615	610	470	211
$H_{c1}(0)$ (Oe)	267	267	147	50
$H_{c2}(0)$ (Oe)	2902	2845	3189	2840
dH_{c2}/dT (Oe/K)	–530	–530	–666	–1020
$\kappa_2(0)$	3.34	3.30	4.8	~8
$\xi(0)$ (Å)	337	340	321	339
$\lambda(0)$ (Å)	1124	1121	1540	2720
a	0.85	0.85	0.55	0.17

experimental accuracy could not be detected in heat capacity measurements. As a result, we will consider the T_c values obtained from heat capacity and magnetization measurements at $H \sim 20$ Oe as the characteristics of bulk superconductivity in the studied YB_6 samples.

C. Magnetization

Figure 7 shows the temperature dependence of magnetic susceptibility $\chi(T) = M(T)/H$ of the YB_6 samples as deduced from magnetization measured at $H_0 = 5.4$ kOe. It is visible from Fig. 7 that in the normal state of YB_6 the susceptibility significantly increases with temperature lowering, changing from negative values at $T > 100$ K to positive ones at low temperatures. As a result, the presence of two additive components in the normal state should be taken into account—the paramagnetic contribution caused by localized magnetic moments of magnetic impurities and the diamagnetic component originating from the YB_6 matrix. It can be discerned in Fig. 7 that the low-temperature component of the paramagnetic susceptibility of samples No. 3 and No. 4 exceeds significantly [~5 times] the $\chi(H, T)$ values of No. 1 and No. 2 crystals.

Below the transition temperature T_c a diamagnetic response is observed on magnetization curves $M(T)$ in small magnetic fields, and this superconducting component corresponds within experimental accuracy to the total Meissner effect (see inset in Fig. 7). An increase of external magnetic field up to 3 kOe leads to the appearance of features on $M(H, T_0)$ curves which are typical for type II superconductors. Indeed, a linear rise of the diamagnetic magnetization is observed in the range below the first critical field $H < H_{c1}$ corresponding to the Meissner phase, and above H_{c1}, in the mixed state, $M(H)$ decreases dramatically until the transition at the second critical field H_{c2} to the normal state occurs. Figure 8 demonstrates the diamagnetic $M(H, T_0)$ dependences as obtained for samples No. 1, No. 3, and No. 4 [panels (a), (b), and (c), respectively]. The procedure usually applied for the extraction of critical fields is shown in the insets of Fig. 8, where the intersection points of linear asymptotics marked as H_{c1} and H_{c2} are shown for various temperatures. The values of H_{c1} were corrected to the demagnetization factor which varies between 1.05 (sample No. 3) and 1.185 (sample No. 1). The received behavior of $H_{c1}(T)$ and $H_{c2}(T)$ for all four studied YB_6 crystals is presented in Fig. 9. It can be seen that the critical fields $H_{c1}(T)$ and $H_{c2}(T)$ for samples No. 1 and No. 2 almost coincide with each other (Fig. 9), while a much smaller $H_{c1}(T)$ and both higher dH_{c2}/dT values of the derivative at T_c and $H_{c2}(0)$ correspond to samples No. 3 and No. 4.

D. Hall and Seebeck coefficients

For samples No. 2, No. 3, and No. 4 the results obtained from Hall resistivity and thermopower measurements are shown in Figs. 10 and 11, respectively; the data are plotted as Hall and Seebeck coefficients $R_H(T)$ and $S(T)$. As can be seen in Fig. 10, the Hall coefficient of YB_6 is negative and its magnitude slightly decreases with decreasing temperature in the range 2–300 K. The absolute values of R_H correspond

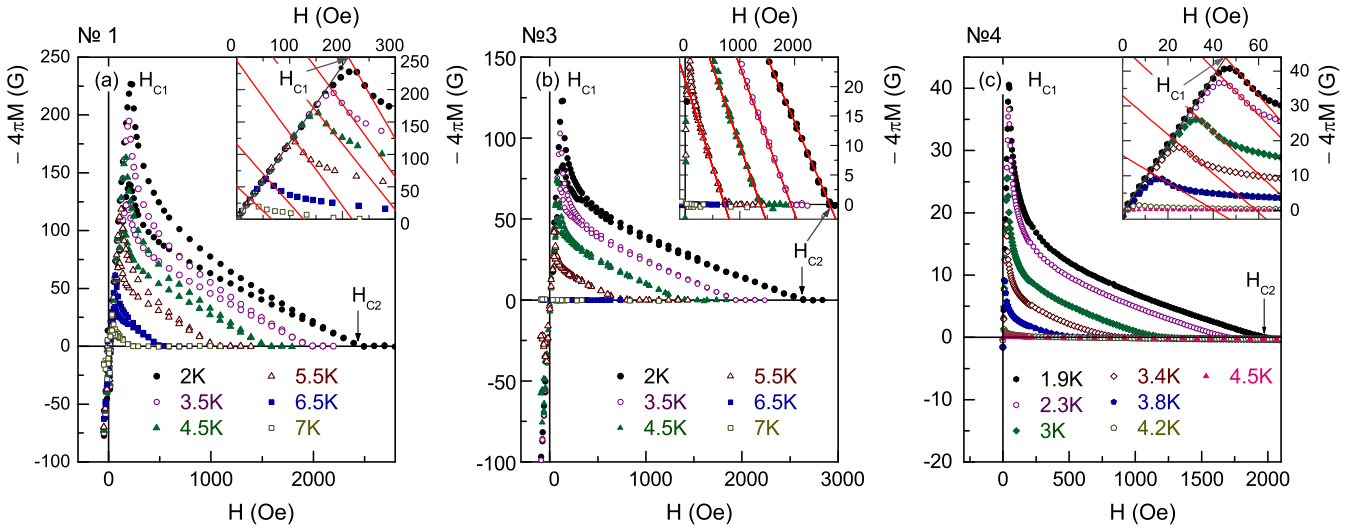

FIG. 8. Magnetic field dependences of magnetization $M(H, T_0)$ in the superconducting state and in the vicinity of the transition temperature for samples (a) No. 1, (b) No. 3, and (c) No. 4. The insets show the procedure for determining the critical fields H_{c1} and H_{c2} (see also text).

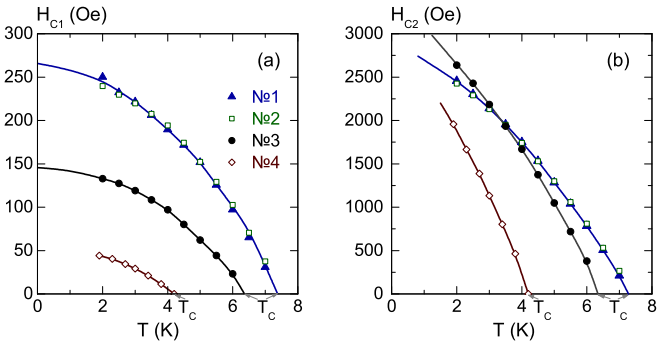

FIG. 9. Temperature dependences of (a) the lower H_{c1} and (b) the upper H_{c2} critical fields for different YB_6 samples resulting from magnetization measurements.

to a carrier concentration $n_e/n_Y = 0.85$–0.95 (where n_Y is the concentration of Y ions) which is slightly below one conduction electron per yttrium ion. Only moderate changes of $R_H(T)$ are observed with the temperature lowering being in the limit of 2.2%, 1.4%, and 3% for crystals No. 2, No. 3, and No. 4, respectively. The most significant decrease of $R_H(T)$ is detected for samples No. 2 and No. 3 in the range between 10 and 50 K corresponding to the steplike anomaly in the temperature dependence of heat capacity (see Fig. 3). Within the limits of experimental accuracy, as the related studies were performed only in fields between 40 and 90 kOe, the data of Fig. 10 do not allow us to discuss the dependence of the Hall coefficient on external magnetic field.

The temperature dependences of the Seebeck coefficient (Fig. 11) demonstrate a typical metallic behavior—the magnitude of $S(T)$ changes from negative values $\sim$1–4.5 μV/K at intermediate temperatures 80–300 K to small alternating ones -0.5–$0.5\,\mu$V/K in the low temperature range. As a result, two main features of thermopower can be detected for samples No. 2 and No. 3: (i) a peak near T_c and (ii) a $S(T)$ maximum in the vicinity of $T^* \sim 50$ K (see Fig. 11) which corresponds to previously discussed anomaly of the Hall coefficient (Fig. 10). In the range between these two

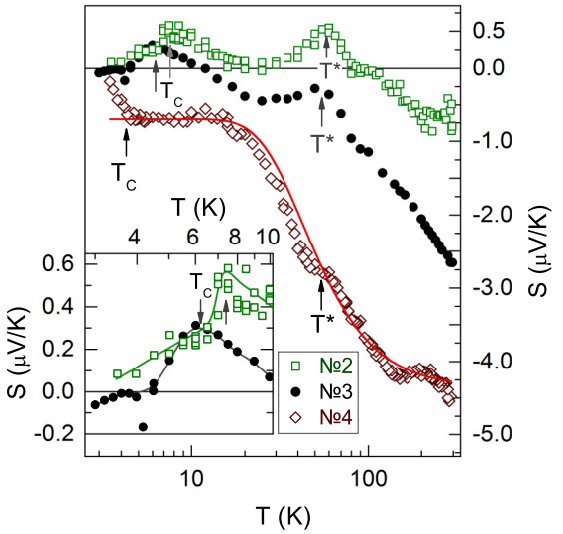

FIG. 11. Temperature dependences of the Seebeck coefficient $S(T)$ for samples No. 2, No. 3, and No. 4. The solid line shows the approximation of $S(T)$ data for sample No. 4 by the phonon-drag thermopower with a single Einstein mode $\Theta_E \approx 150$ K (see Fig. S2 in Ref. [28] for more details). The inset shows an enlarged area near the superconducting transition temperature T_c. The arrows indicate T_c and the transition to the cage-glass phase (T^*).

features a minimum on $S(T)$ curves is observed. Instead of a peak on $S(T)$ dependence a shoulder can be identified at T^* for sample No. 4 in combination with a steplike anomaly in the range $T < 150$ K. Then, in the superconducting state, the thermopower decreases sharply to close to zero values (see also inset in Fig. 11) which are typical for superconductors [29].

IV. DISCUSSION

A. Characteristics of the superconducting state of YB_6

1. Analysis of specific heat

The specific heat results in the normal and superconducting states [Figs. 3 and 4] were used to determine the

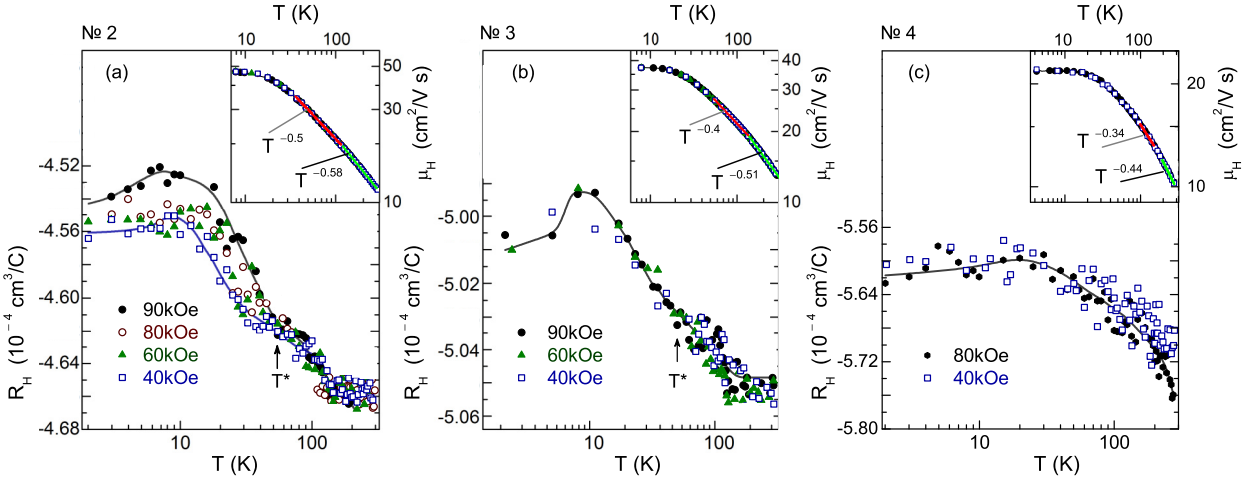

FIG. 10. Temperature dependences of the Hall coefficient $R_H(T)$ obtained for samples (a) No. 2, (b) No. 3, and (c) No. 4 of YB_6 at different magnetic fields 40–90 kOe. The arrows at T^* indicate the phase transition to the cage-glass state. The insets show the temperature dependence of the Hall mobility $\mu_H(T) = R_H(T)/\rho(T)$. The solid lines in the insets demonstrate the approximation of the Hall mobility by power law dependence $\mu_H(T) \sim T^{-\alpha}$ (see text).

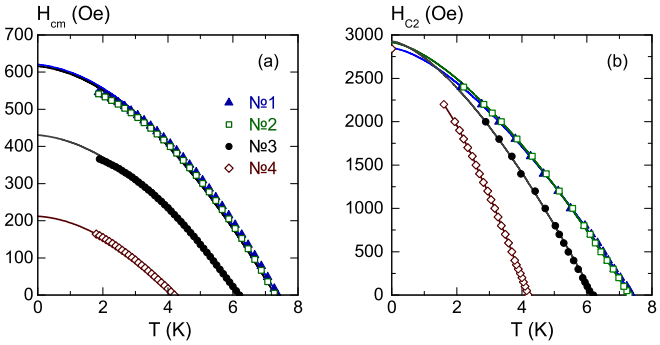

FIG. 12. Temperature dependences of (a) the thermodynamic $H_{\rm cm}$ and (b) the upper H_{c2} critical fields for different YB_6 samples resulting from specific heat measurements. The solid lines show the data approximation by Eqs. (4) and (5).

thermodynamic critical field $H_{\rm cm}(T)$ within the framework of standard relations

$$-\tfrac{1}{2}\mu_0 V H_{\rm cm}^2(T) = \Delta F(T) = \Delta U(T) - T\Delta S(T) \quad (1)$$

$$\Delta U(T) = \int_T^{T_c} [C_s(T') - C_n(T')]dT' \quad (2)$$

$$\Delta S(T) = \int_T^{T_c} \frac{[C_s(T') - C_n(T')]}{T'} dT', \quad (3)$$

where F and U denote the free and internal energies, S—the entropy, V—the molar volume, and the indices n and s correspond to characteristics of the normal and superconducting phases of YB_6. The integration was carried out in the temperature range from T to T_c. Before the integration the specific heat data in the normal and superconducting states were approximated by polynomials of the fourth order. Figures 12(a) and 12(b) show the dependences of the thermodynamic $H_{\rm cm}(T)$ and upper critical fields $H_{c2}(T)$, respectively, resulting from the heat capacity analysis of studied crystals. Table I presents the $H_{\rm cm}(0)$ values obtained by extrapolation of $H_{\rm cm}(T)$ curves in the framework of the standard Bardeen-Cooper-Schriffer (BCS) relation

$$H_{\rm cm}(T)/H_{\rm cm}(0) = 1.7367(1 - T/T_c)[1 - 0.327(1 - T/T_c) - 0.0949(1 - T/T_c)^2]. \quad (4)$$

In addition, Table I presents also the derivatives dH_{c2}/dT at $T = T_c$ obtained from experimental data and the upper critical field $H_{c2}(0)$ defined within the framework of formula used in Ref. [30]

$$H_{c2}(0) = -0.69T_c\left(\frac{dH_{c2}}{dT}\right)_{T=T_c}. \quad (5)$$

Using the value of the electronic specific heat coefficient $\gamma \approx 3.8$–3.85 mJ/(mol K^2) received for crystals No. 1 and No. 2 [see Fig. 5(a)], the density of electronic states at the Fermi level $N_b(E_F) = 0.119$ (eV atom)$^{-1}$ known from band structure calculations [31,32] and the relation $\gamma = 1/3\pi^2 k_B^2 N_b(E_F)(1 + \lambda_{\text{e-ph}})$ (k_B—Boltzmann constant), we estimate the electron-phonon interaction constant $\lambda_{\text{e-ph}} = 0.93$–$0.96$ in good agreement with results of [3]. On the contrary, a strongly reduced value of $\lambda_{\text{e-ph}} \approx 0.32$ can be deduced from $\gamma \approx 2.59$ mJ/(mol K^2) observed for crystal No. 4 [see Fig. 5(b)].

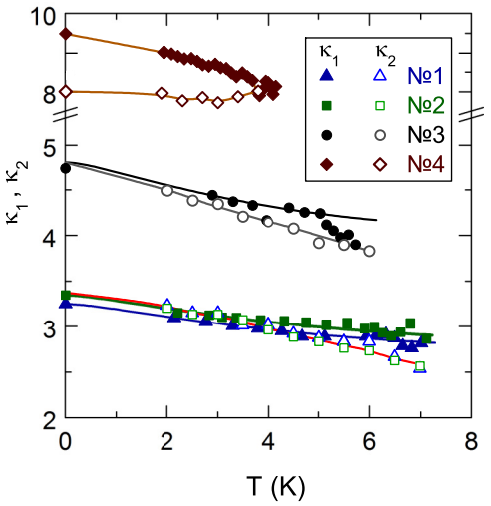

FIG. 13. Temperature dependence of the Ginzburg-Landau-Maki parameters obtained from measurements of heat capacity (κ_1) and magnetization (κ_2) of different YB_6 samples.

Then, from BCS relations

$$\Delta(0) = \frac{H_{\rm cm}(0)}{\sqrt{2\pi N(E_F)}} \quad (6)$$

$$\xi(0) = \sqrt{\frac{\Phi_0}{2\pi H_{c2}}} \quad (7)$$

$$\kappa_1(T) = \frac{H_{c2}(T)}{\sqrt{2}H_{\rm cm}(T)}, \quad (8)$$

where Φ_0 denotes the flux quantum, the Ginzburg-Landau-Maki parameter $\kappa_1(T)$ [33] (Fig. 13), the superconducting gap $\Delta(0)$, the coherence length $\xi(0)$, and the penetration depth $\lambda(0) = \kappa_1(0) \cdot \xi(0)$ [Table I] could be calculated. For sample No. 3, due to the presence of a magnetic contribution to heat capacity (see Fig. 5) and the associated problem with the determination of the Sommerfeld coefficient, the estimation of γ was obtained from the relation $\gamma T_c^2/H_{\rm cm}^2(0) = const$ [3]. Thus, for sample No. 3 we obtained $\gamma \approx 2.94$ mJ/(mol K^2) and $\lambda_{\text{e-ph}} = 0.5$ detecting a strong reduction of the electron-phonon interaction in this YB_6 crystal. The ratio of $2\Delta/k_BT_c \approx 3.9$–$4$ found in this study for No. 1–No. 3 YB_6 samples coincides with results obtained both in Ref. [3], from the heat capacity analysis and from the point-contact and tunnel spectra of Refs. [34,35], and it significantly exceeds the value of 3.52 of the BCS model. On the contrary, a small enough value of $2\Delta/k_BT_c \sim 3$ was detected for sample No. 4. It is also worth noting that the smaller values of $2\Delta/k_BT_c \approx 3.8$ found in Ref. [36] and 3.6 in Ref. [37] from ultrahigh resolution photoemission spectra at 5 K and tunneling spectra at 4.3 K, respectively, obviously may be attributed to gap $\Delta(T)$ lowering at about 5 K (close to $T_c \approx 7$ K) in comparison with $\Delta(0)$.

TABLE III. Characteristics of charge carriers scattering in YB_6: ρ_0—residual resistivity, n_e—concentration of charge carriers, τ_e—relaxation time of conduction electrons, v_F—average Fermi velocity, l—mean free path of conduction electrons.

	No. 1	No. 2	No. 3	No. 4
ρ_0 ($\mu\Omega$ cm)	8.28	9.68	13.35	25.6
n_e ($\times 10^{22}$ cm^{-3})	1.4	1.38	1.25	1.12
τ_e ($\times 10^{-14}$ s)	2.8	2.75	2.2	1.3
v_F ($\times 10^7$ cm/s)	2.07	2.02	1.42	0.88
l (Å)	58	55.5	31.1	11.3

2. *Analysis of magnetization*

The analysis of magnetization was carried out based on formulas which are well known from the Abrikosov theory of type-II superconductivity [38]

$$-4\pi M = (H_{c2} - H)/\left[\left(2\kappa_2^2 - 1\right)\beta_\Delta\right] \tag{9}$$

$$H_{c1}(T) = H_{c2}/2\kappa_2^2(\ln\kappa_2 + a), \tag{10}$$

where κ_2 is the Ginzburg-Landau-Maki parameter [33,39], $\beta_\Delta = 1.16$ the coefficient corresponding to a triangular lattice of Abrikosov vortices, and a the constant depending on impurity concentration. Presented in Fig. 8 are the linear dependences of magnetization $M(H)$ in the superconducting phase near H_{c2} which allow us to derive the $\kappa_2(T)$ behavior within the framework of Eq. (9) [see Fig. 13]. Then, the extrapolation to zero temperature provides the values of $\kappa_2(0)$ and a parameters. In addition, the use of relation (7) allows us to estimate the coherence length $\xi(0)$ and the penetration depth $\lambda(0) = \kappa_2(0) \cdot \xi(0)$ (see Table II).

The comparison of Ginzburg-Landau-Maki parameters $\kappa_1(T)$ and $\kappa_2(T)$ [33,38,39] for crystals No. 1–No. 3 obtained from the analysis of heat capacity [Eq. (8)] and magnetization [Eq. (9)], respectively, shows that κ_1 and κ_2 differ mainly near T_c, but their characteristics are practically identical at temperatures below $T_c/2$ (Fig. 13) resulting in the relation $\kappa_1 \geqslant \kappa_2$ for temperatures below T_c. However, according to Refs. [39,40] in case of a superconductor in the "dirty limit" an opposite inequality $\kappa_1 \leqslant \kappa_2$ is expected for any relation between the mean free path l of charge carriers and the coherence length ξ. Our estimates of l from residual resistivity ρ_0, from the Hall coefficient R_H, and from parameters $\xi(0)$ and $\Delta(0)$ lead within the framework of standard relations

$$l = R_H m^* v_F/(e\rho_0) \tag{11}$$

$$\xi(0) = \hbar v_F/[\pi\Delta(0)] \tag{12}$$

(where v_F is the average Fermi velocity and m^* the effective mass, $m^* = 1.03m_0$ [41]) to values of $l = 11$–58 Å for the studied crystals (see Table III). This results also in inequality $l \ll \xi$ that validates the "dirty limit" for superconductivity in YB_6. Note that both the Fermi velocity $v_F \approx 0.9$–2.1×10^7 cm/s and the relaxation time of charge carriers $\tau_e \approx 1.3$–2.8×10^{-14} s derived here (Table III) are in good agreement with the estimates obtained for YB_6 in μSR [42] ($v_F \sim 10^7$ cm/s) and in optical conductivity [43]

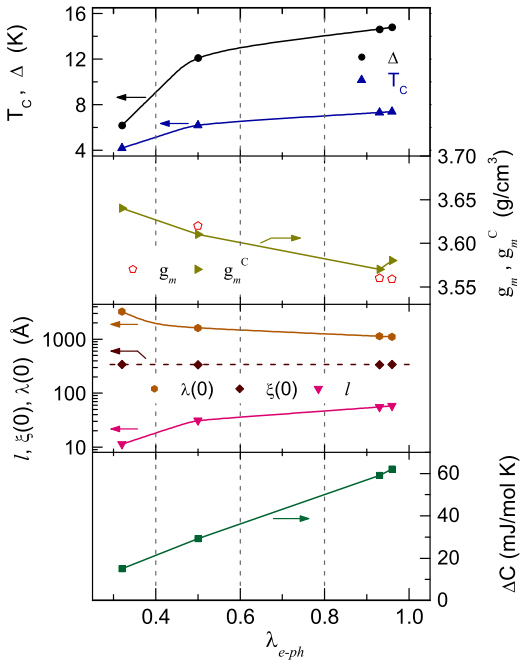

FIG. 14. ξ, λ, and l parameters as a dependence of electron-phonon interaction constant $\lambda_{e\text{-}ph}$ in studied YB_6 crystals. Information about variations of the transition temperature $T_c(\lambda_{e\text{-}ph})$, the superconducting gap $\Delta(\lambda_{e\text{-}ph})$, the heat capacity jump $\Delta C(\lambda_{e\text{-}ph})$ at T_c, and the mass densities g_m, $g_m^C(\lambda_{e\text{-}ph})$ for the samples No. 1–No. 4 also summarized in this figure.

($\tau_e \approx 2.1 \times 10^{-14}$ s at $T = 9$ K) studies. It is also worth noting that for type-II superconductors in the dirty limit $\xi \gg l$ the relation

$$\kappa_d = \kappa_p + 7.53 \times 10^3 \rho_0 \gamma^{1/2} \tag{13}$$

(see, e.g., [40]) may be applied for $\kappa_d \gg \kappa_p$ (κ_d and κ_p are Ginzburg-Landau-Maki parameters in the dirty and pure limits, correspondingly) to carry out the "upper limit" estimation of γ. Knowing the residual resistivity ρ_0 and κ_2 for sample No. 3 (see Tables II and III) we obtain $\gamma \approx 3.02$ mJ/(mol K^2), which is in good agreement with our previous result $\gamma \approx 2.94$ mJ/(mol K^2). Figure 14 shows ξ, λ, and l as a dependence of the electron-phonon interaction constant $\lambda_{e\text{-}ph}$ in studied YB_6 crystals. In Fig. 14 we summarize also information about the transition temperature $T_c(\lambda_{e\text{-}ph})$, the superconducting gap $\Delta(\lambda_{e\text{-}ph})$, the jump $\Delta C(\lambda_{e\text{-}ph})$ of heat capacity at T_c, and about the mass densities g^m, $g_m^C(\lambda_{e\text{-}ph})$ of samples No. 1–No. 4. It can be seen that all these characteristics except ξ change monotonously with $\lambda_{e\text{-}ph}$ and their variation becomes faster when the electron-phonon interaction decreases below 0.5. The reasons for this kind behavior are discussed in the next section. Additionally, our temperature variation of $\kappa_1(0)/\kappa_1(T_c) \approx 1.16$ found for samples No. 1–No. 3 coincides with the result of Ref. [3]. At the same time the obtained $\kappa_1(T)$ changes are smaller than these of $\kappa_2(T)$ and the corresponding ratio is $\kappa_2(0)/\kappa_2(T_c) \approx 1.32$. The $\kappa_2(T)$ behavior is practically invariant for all samples changing in contradiction with the previous theoretical and experimental results (see, e.g., Refs. [39,40]). Indeed, although according to Ref. [39] the differences in the behavior of κ_1 and κ_2 should depend both on the ratio ξ/l, and

also on the anisotropy of carrier scattering by impurities, but at T_c the equality $\kappa_1 \approx \kappa_2$ should be valid. Thus, the obtained relation $\kappa_1(T_c) > \kappa_2(T_c)$ in YB_6 (Fig. 13) is not consistent with the conclusion of Ref. [39], as well as the changes of the Ginzburg-Landau-Maki parameters $\kappa_1(0)/\kappa_1(T_c) \approx 1.16$ and $\kappa_2(0)/\kappa_2(T_c) \approx 1.32$ are not in accordance with the results [39] of numerical calculations for superconductors in the "dirty limit" (for YB_6 $\xi/l = 6$–30, see Tables I, II, III). At the same time, it should be taken into account that the behavior of the thermodynamic H_{cm} and the upper critical field H_{c2} is almost identical for all investigated samples [Fig. S3 in Ref. [28] shows the scaling of $H_{cm}(T)$ and $H_{c2}(T)$ dependences]. Hence, for various YB_6 samples distinguished by T_c, by residual resistivity and the paramagnetic contribution to magnetic susceptibility [Fig. 7], it is necessary to look for a common mechanism responsible for the decrease of the Ginzburg-Landau-Maki parameter κ_2 in comparison with the $\kappa_1(T)$ behavior near T_c. The relation between the Ginzburg-Landau-Maki parameters $\kappa_1(T_c) > \kappa_2(T_c)$ found in this study can be explained within the framework of the approach suggested by Maki [33] which additionally takes into account the strong Pauli paramagnetism in the presence of spin-orbit interaction. Such an unusual relation $\kappa_1(T) > \kappa_2(T)$ was observed previously by authors of Ref. [44] in alloys $Nb_{0.5}Ta_{0.5}$ and $In_{0.981}Bi_{0.019}$ near T_c. Apparently, the emergence and the strengthening in external magnetic field of the spin polarization of electron states may be considered also as the mechanism which is responsible for the different behavior between the κ_1 and κ_2 parameters observed in yttrium hexaboride.

At the end of this section, it is worth noting that in accordance with calculations performed in Ref. [45] for superconductors with a strong electron-phonon interaction, the parameter $\gamma T_c^2/H_{cm}^2(0)$ depends on the ratio T_c/Θ_E (Θ_E—Einstein temperature, $\Theta_E \approx 8$ meV for YB_6) and that this ratio can be used to classify the type of Cooper's pairing. As a result, for YB_6 with $T_c/\Theta_E \sim 0.075$ we found the ratio $\gamma T_c^2/\mu_0 V H_{cm}^2(0) \approx 1.7$ (μ_0—magnetic constant) which is approximately twice lower than the value (~3.7) predicted in [45] for d-wave pairing. This supports the expected s-type superconductivity in YB_6.

B. Characteristics of the normal state of YB_6

1. *Specific heat at H = 5 kOe*

In the analysis of normal state heat capacity contributions of YB_6 we used the approach similar to that employed earlier [2,46–50] in studies of higher borides of rare earth elements. In addition to the electronic component $C_{el} = \gamma T$ with $\gamma \approx 3.8$ mJ/(mol K^2) [for samples No. 1 and 2], $\gamma \approx 2.94$ mJ/(mol K^2) [for sample No. 3], and $\gamma \approx 2.59$ mJ/(mol K^2) [for sample No. 4], and the Debye C_D contribution which originates from the rigid covalent framework of boron atoms

$$C_D = 9rR\left(\frac{T}{\Theta_D}\right)^3 \int_0^{\Theta_D/T} e^x x^4 [e^x - 1]^{-2} dx \qquad (14)$$

(for RB_6 $r = 6$, R is the universal gas constant, Θ_D the Debye temperature), in this case also the Einstein C_E component of the specific heat

$$C_{E_i} = 3RN_{E_i}\left(\frac{\Theta_{E_i}}{T}\right)^2 \exp\left(\frac{\Theta_{E_i}}{T}\right)\left[\exp\left(\frac{\Theta_{E_i}}{T}\right) - 1\right]^{-2} \qquad (15)$$

[N_{E_i}—number of oscillators per unit cell ($i = 1, 2$)], has to be taken into account. The C_{E_i} term (15) is caused by quasilocal vibrations of yttrium ions located in the cavities formed by boron B_{24} cubooctahedra and loosely bound to the rigid covalent boron sublattice. Equations (14) and (15) allowed us to estimate both the Einstein ($\Theta_{E_1} \approx 97.2$ K) and Debye ($\Theta_D \approx 1160$ K) temperatures of samples No. 1–No. 4. For example, Figs. 15(a) and 15(b) present in coordinates $(C - \gamma T - C_D)/T^3$ vs T the low temperature heat capacity of investigated YB_6 crystals. The received value $\Theta_{E_1} \approx 97.2$ K is consistent with the results of point-contact [34] and tunneling [35] spectroscopy measurements ($\omega_E \sim 8$ meV), and with inelastic neutron scattering ($\omega_E \sim 10$ meV) [51] and Raman scattering ($\omega_E \sim 70$ cm^{-1}) [52] data. The value

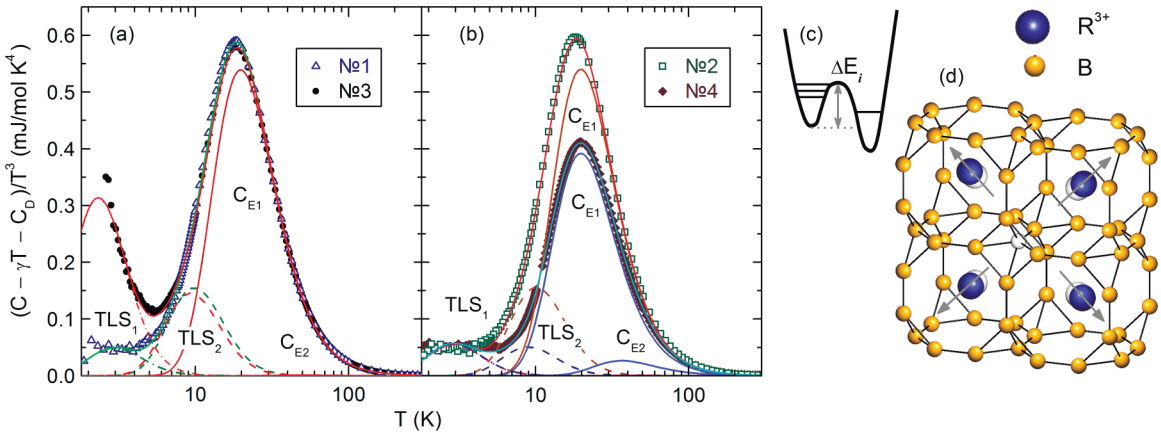

FIG. 15. (a), (b) Separation of the contributions to the low temperature heat capacity $(C - \gamma T - C_D)/T^3$ in the normal state ($H_0 = 5$ kOe): The Einstein (C_{E_1}, C_{E_2}) components and two types of vacancy (TLS_1, TLS_2) components are shown by the solid and dashed lines, respectively. (c) Schematic representation of the double-well potential with a barrier height ΔE_i. (d) Crystal structure of YB_6. The presence of boron vacancy (shown as a white ball in the center) offsets (represented by arrows) four nearest yttrium R^{3+} ions from their centrosymmetric positions in the cubooctahedrons B_{24}.

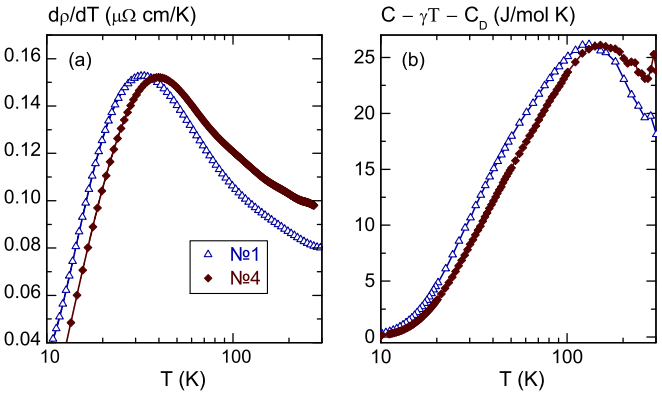

FIG. 16. Temperature dependences of (a) resistivity derivative $d\rho/dT$ and (b) heat capacity $(C - \gamma T - C_D)$ vs T for crystals No. 1 and No. 4.

$\Theta_D \approx 1160$ K coincides with the results of heat capacity calculations for LaB_6 [46–49]. It is also in agreement with the data of $\Theta_D \approx 1160$–1190 K obtained in [2,50,53] for the analog nonmagnetic higher boride—lutetium dodecaboride (LuB_{12}), and comparable to $\Theta_D \approx 1250$–1370 K deduced for β boron in x-ray diffraction studies [53]. For crystal No. 4 the above mentioned shift of the steplike $C(T)$ anomaly is accompanied by the appearance of additional heat capacity at temperatures in the range 140–300 K [see Fig. 16(b) for more details]. As a result, the C/T^3 versus T plot shows a strong amplitude reduction of the main bell-shape maximum corresponding to $\Theta_{E_1} \approx 97.2$ K in combination with the appearance of an additional Einstein heat capacity component with $\Theta_{E_2} \approx 180$ K [see also Fig. 15(b)].

Along with these Einstein components, which lead to maxima on $(C - \gamma T - C_D)/T^3$ vs T curves near 20 K and 35 K [see Figs. 15(a) and 15(b)], we observed two additional features on these dependences—one near 10 K and another below 4 K. The separation of these low-temperature contributions was made in the same manner as it was done for LaB_6 in Refs. [48,49], where the heat capacity below 20 K was associated with two additive two-level systems (TLS) attributed to vibrations of rare earth ions in the vicinity of boron vacancies (see TLS_1 and TLS_2 in Figs. 15(a), 15(b) and also Ref. [54]). These two TLS terms were described by the Schottky formula

$$C_{\mathrm{Sh}_i} = RN_i g_{0i} g_{1i} \left(\frac{\Delta E_i}{T}\right)^2 \exp\left(\frac{\Delta E_i}{T}\right) \times \left[g_{0i} \exp\left(\frac{\Delta E_i}{T}\right) + g_{1i}\right]^{-2}, \quad (16)$$

where g_{0i}, g_{1i} denote the degeneracy of the ground and excited states, ΔE_i the splitting energy, and N_i the concentration of the two-level systems (TLS). The analysis of the low temperature heat capacity $(C - \gamma T - C_D)/T^3$ of LaB_6 was undertaken in Refs. [48,49] in the framework of relation (16) for three different schemes of levels, including **3–1**, **1–1**, and **1–3** configurations. As a result, describing the heat capacity of La^NB_6 with various boron isotopes ($N = 10, 11, nat$) authors [48,49] choose TLS diagrams consisting of singlet and triplet states, which allowed them to obtain the best fit with the lowest concentration of boron vacancies in the hexaboride compounds.

TABLE IV. Parameters of the heat capacity $(C - \gamma T - C_D)/T^3 = f(T)$ (Fig. 15) approximation by formulas (15) and (16): ΔE_1, ΔE_2 and N_1, N_2 are the height of barriers and the reduced concentrations of double-well potentials TLS_1 and TLS_2, respectively; N_{E1}, N_{E2}, and N_E are the reduced concentrations of Einstein oscillators. We present also the chemical composition found for the investigated YB_6 crystals and the mass densities g_m^C and g_m obtained from $C(T)$ and hydrostatic measurements, respectively.

	No. 1	No. 2	No. 3	No. 4
ΔE_2 (K)	51	52.4	48.4	46.2
$N_2 = 4n_v$	0.041	0.044	0.033	0.01
ΔE_1 (K)	15.3	15	12.1	15
$N_1 \sim n_d$	0.00035	0.00037	0.00107	0.00038
N_{E_1}	0.93	0.932	0.932	0.676
N_{E_2}	0.02	0.013	0.028	0.294
N_E	0.95	0.945	0.96	0.97
Chemical composition from $C(T)$	$Y_{0.95}B_{5.94}$	$Y_{0.945}B_{5.933}$	$Y_{0.96}B_{5.95}$	$Y_{0.97}B_{5.985}$
g_m^C (g/cm^3)	3.58	3.57	3.61	3.64
g_m (g/cm^3)	3.559 ± 0.006	3.56 ± 0.01	3.62 ± 0.02	[a]

[a]The size of crystal No. 4 was too small to carry out its precise hydrostatic density measurement.

We emphasize that the presence of boron vacancies has been clearly confirmed in x-ray and neutron studies of RB_6, and it was shown in Refs. [55–58] that there are about 1–9% of vacancies in the boron sublattice in all known hexaborides. The concentration of these defects depends both on the R ion and the method of the single crystal growth. The presence of boron vacancies, on one side, and the loosely bound states of R ions in the rigid covalent boron framework, on the other side, lead to displacements of the R^{3+} ions from their centrosymmetric positions inside the truncated B_{24} cubooctahedra [see Fig. 15(d)]. This gives rise to a disorder in the arrangement of yttrium ions in the hexaboride matrix. The derangement increases with temperature lowering, and depending on the concentration of intrinsic defects and impurities, a number of nonequivalent positions is expected for R^{3+} ions in RB_6. Thus, similar to amorphous compounds and glasses [59], in the cage-glass configuration the appearance of two level systems is related to the disorder in the arrangement of heavy ions in RB_6 crystals. In other words, the emergence of TLS seems to be equivalent to the formation of different double-well potentials with a barriers ΔE_i [Fig. 15(c)]. It is worth noting that the bell-shape anomaly is well known in glasses as the boson peak, and it is usually centered at temperatures 10–30 K in the plot of C_{ph}/T^3 versus T [60–74].

Following the approach, the low-temperature data C/T^3 of YB_6 [Figs. 15(a) and 15(b)] have been approximated by Eqs. (15) and (16) with two Einstein contributions C_{E_1} ($\Theta_{E_1} \approx 97.2$ K) and C_{E_2} and two types of two-level systems TLS_i ($i = 1, 2$) each consisting of singlet ($g_{0i} = 1$) and triplet ($g_{1i} = 3$) states. The barrier height of TLS_2 [see Fig. 15(c) and Table IV] was found to be $\Delta E_2 \sim 50$ K, and this value does not strongly depend on the concentration

TABLE V. Parameters of the magnetic susceptibility χ(T) approximation by Eq. (17): N_{m0}—concentration of magnetic centers per unit cell, μ_{eff}—the effective magnetic moment of magnetic centers, χ_d—diamagnetic contribution to susceptibility. The concentration of ytterbium impurities x(Yb) in YB_6 samples detected from spectral analysis data is also presented.

		$\chi(T, H_0 = 5.4$ kOe)			
YB_6	x_{Yb} (ppm)	$N_{m0}\,\mu_{\text{eff}}^2$ (emu/mol)	$N_1 = N_{m0}$ (f.u.)	μ_{eff} (μ_B)	χ_d ($\times 10^{-5}$ emu/mol)
No. 1	10	0.00344	0.00035	3.14	−3.8
No. 2	10	0.00288	0.00037	2.79	−4.8
No. 3	200–1000	0.0144	0.00107	3.67	−2.6
No. 4	100	0.0069	0.00038	4.26	−0.25

of intrinsic defects in crystals No. 1–No. 4. The obtained relative concentration of cells with a double-well potential was found to be $N_2 \approx 0.01$–0.044, and similar as in the case of LaB_6 [48,49], it may be associated with the number of boron vacancies in the YB_6 structure. Each vacancy namely produces a displacement of yttrium ions from their centrosymmetric positions in four neighboring B_{24} clusters [see Fig. 15(d)], so the right concentration of boron vacancies should be $n_v(B) = N_2/4 \approx 0.25$–$1.1\%$, indicating a decrease of mass density in studied YB_6 single crystals. The observed concentration of TLS_1 in crystals No. 1, No. 2, and No. 4 ($\Delta E_1 \approx 15$ K, $N_1 \approx 0.35$–0.38×10^{-3}, Table IV) is quite small when compared with the number of boron divacancies $N_1 \approx 0.9$–1×10^{-3}, previously detected in LaB_6 [48,49]. Then, the estimation of the concentration of boron divacancies in case of their random distribution in the RB_6 matrix leads to $n_d(\text{B}) = n_v(\text{B})(1 - [1 - n_v(\text{B})]^z) \approx 0.4$–$0.5 \times 10^{-3}$ (where $z = 4$ is the coordination number in the boron sublattice), which is for crystals No. 1 and No. 2 in a reasonable compliance with the TLS_1 concentration N_1 (Table IV). On the contrary, the value of TLS_1 concentration $N_1 \approx 1.07 \times 10^{-3}$ for crystal No. 3 (see Table IV) exceeds significantly the estimated $n_d(\text{B}) \approx 0.26 \times 10^{-3}$, and seems to indicate the formation of complexes of boron vacancies in this YB_6 crystal. Note that the number of yttrium vacancies [$n_v(\text{Y}) = 1 - N_E \approx 3$–$5.5\%$, Table IV] is also detected from the heat capacity analysis and contributes to the mass density lowering in YB_6.

2. *Analysis of magnetic susceptibility*

The analysis of contributions to magnetic susceptibility of samples No. 1–No. 4 in the normal state [Fig. 7] was carried out in the framework of relation

$$\chi = M/H = \mu_{\text{eff}}^2 N_{m0}/(3k_B T) + \chi_d, \qquad (17)$$

where N_{m0} is the concentration of magnetic centers in small magnetic fields, χ_d the diamagnetic susceptibility. Figure 7 shows the fitting results of the experimental curves $\chi(T)$ by Eq. (17) indicating that within the limits of experimental accuracy the susceptibility follows the Curie dependence. Table V presents the parameters obtained by this approximation.

It is worth noting that the localized magnetic moments with concentrations of N_{m0}, determine the paramagnetic susceptibility of YB_6 (Fig. 7), correspond to small fields [$H = 5.4$ kOe, linear $M(H)$ dependence]. It was found from the optical emission spectral analysis that the magnetic impurity doping level in the samples No. 1 and No. 2 is about 10 ppm. Hence, in the absence of magnetic impurities the detected magnetic moments may be associated with complexes of vacancies in the matrix of this nonmagnetic hexaboride. It should be mentioned that although in strong magnetic fields the low temperature magnetic contribution to heat capacity within the experimental accuracy could not be clearly detected in crystals No. 1 and No. 2 [Fig. 5(a)], the presence of a small amount of complexes of vacancies ($N_1 = 350$–370 f.u.~ 50 ppm, see Tables IV and V) in these two samples can account for their Curie dependence of magnetic susceptibility $\chi(T)$ (Fig. 7). In this case the strong increase (~ 5 times) of concentration of divacancies N_1 in sample No. 3 ($N_1 = 1070$ f.u. ~ 150 ppm, Table IV) compared with No. 1 and No. 2 leads in small fields to a proportional elevation of the paramagnetic response (Fig. 7 and Table V). Thus, within the approach the complexes of vacancies in the YB_6 matrix are responsible both for the appearance of the low temperature heat capacity component [TLS_1 in Figs. 15(a) and 15(b)] and for the emergence of the paramagnetic Curie term in the magnetic susceptibility $\chi(T, H_0 = 5.4$ kOe) (Fig. 7). Taking the concentration $N_{m0} = N_1$ from the analysis of heat capacity at $H = 5$ kOe and the $N_{m0}\mu_{\text{eff}}^2$ parameter obtained from the susceptibility approximation by relation (17), we can estimate the value of the magnetic moment of these magnetic complexes $\mu_{\text{eff}} = 2.8$–$4.3\ \mu_B$ for No. 1–No. 4 crystals (Table V).

The calculated value of the magnetic moment $\mu_{\text{eff}} \approx 2.36\ \mu_B$ obtained in Ref. [75] for clusters of boron vacancies in RB_6 serve in favor of this interpretation. It is worth noting also that in Ref. [76] weak magnetic states were predicted in two-dimensional boron composed of B_{20} clusters in a hexagonal arrangement. In addition, suppression of superconductivity due to the formation of magnetic moments in the vicinity of nonmagnetic Lu impurities has been recently found in $Zr_{1-x}Lu_xB_{12}$ [77] and associated with the spin polarization of d states in the conduction band. In favor of this alternative spin-polaron scenario points, e.g., the weak ferromagnetism of charge carriers observed both in some nonmagnetic hexaborides as $Ca_{1-x}La_xB_6$, $Ca_{1-x}Ba_xB_6$ [78,79] and in the paramagnetic phase of PrB_6 [80,81].

It should be mentioned here that contrary to the case of samples No. 1 and No. 2, the spectral analysis shows that the crystal No. 3 contains 200–1000 ppm of ytterbium impurities. Thus, compared with samples No. 1 and No. 2, a large magnetic contribution to the heat capacity and magnetic susceptibility of crystal No. 3 may at first glance be associated with magnetic Yb^{3+} impurities. However, it was shown in Refs. [82–84] that Yb ions are divalent and nonmagnetic in the RB_6 matrix. Moreover, in diamagnetic YbB_6 compound

the concentration of magnetic Yb^{3+} ions is very small and varies within 0.1–2%. Thus, even if taking into account the presence of about 1000 ppm of ytterbium impurities (the upper limit found by the spectral analysis in sample No. 3), there seem to be no more than 20 ppm of magnetic Yb^{3+} centers. As a result, the estimated concentration of magnetic centers 350–1070 f.u. (= 50–150 ppm) with effective moment $\mu_{\text{eff}} \sim 3$–$4\ \mu_B$ serves as an argument against the explanation of the magnetic contribution to heat capacity and of magnetization in terms of YB_6 doping by Yb^{3+} magnetic impurities. Moreover, it also seems to allow excluding a direct correlation between the concentration of ytterbium impurities and the value elevation of residual resistivity in YB_6. The analysis of the low temperature magnetic heat capacity component C_m of sample No. 3 (see Fig. S1 in Ref. [28] for details) allows us to assume that the magnetic TLS_m term may be caused by high spin configurations of strongly distorted B_6 molecules in nonequilibrium crystals of YB_6. In particular, the small g-factor value of this Schottky component ($g = 0.51 \pm 0.02$, see Fig. S1(d) in Ref. [28]) serves as an argument in favor of this interpretation. The comparison of the concentration of magnetic impurities $N_{m0} \sim 150$ ppm in YB_6 sample No. 3 ($T_c = 6.6$ K) with the concentration of magnetic impurities $N_{m0} \sim 50$ ppm of crystal No. 4 with a much smaller $T_c = 4.2$ K (see Tables IV and V) allows us to conclude that the magnetic impurity induced pair-breaking effect cannot be considered as the main reason of the T_c suppression in YB_6 (see Fig. 14). At the end of this section it is worth noting that in our experimental study also attempts were undertaken to measure the field dependence of magnetization of all No. 1–No. 4 crystals with the help of the PPMS-9. However, the signal from sample holder which was comparable with the magnetization of sample No. 3 did not allow us to carry out the separation and analysis of contributions in strong magnetic fields.

3. *Anomalies of charge transport and of thermodynamic parameters near T**

The formation of two-level systems in higher borides was for the first time observed experimentally in rare earth dodecaborides LuB_{12} [2] and ZrB_{12} [50] which are composed of a rigid framework formed by boron nanoclusters B_{12} and heavy ions embedded in cavities arranged by B_{24} cubooctahedra. In Raman spectra of single crystalline Lu^NB_{12} [2] and Zr^NB_{12} [85] samples with a different isotopic composition of boron ($N = 10$, 11, *nat*) it was shown that the Raman response exhibits a boson peak at liquid nitrogen temperatures and such a feature in the low-frequency range is a fingerprint of systems with strong structural disorder. To explain the properties of LuB_{12}, the authors of Ref. [2] have proposed a model of cage-glass formation with a phase transition at $T^* \sim 50$–70 K, and it was found that the barrier height of the double-well potential ΔE [Fig. 15(c)] is practically equal to the cage-glass transition temperature T^*. Moreover, it has been shown very recently [86] that there is an extra source of lattice instability in LuB_{12} related to the Jahn-Teller effect of B_{12} clusters, which manifests the displacements of Lu atoms in oversized B_{24} cages and results in cooperative dynamic Jahn-Teller lattice distortions and conduction band changes. Similar effects are expected in the other higher borides, including hexaborides. As a result, the temperature lowering at $T < T^*$ leads to displacements of metallic ions from their centrosymmetric positions inside the B_{24} cubooctahedra [see, e.g., Fig. 15(d) for RB_6]. The result is a static disorder in the arrangement of R^{3+} ions while maintaining the rigid covalent boron framework. The presence of two-level systems with a barrier $\Delta E \sim 90$ K was reliably demonstrated also in LaB_6 and in $Ce_xLa_{1-x}B_6$ solid solutions based on low-temperature heat capacity measurements [48,49]. Furthermore, a pseudogap [87] and a low-frequency peak in inelastic light scattering spectra [88,89] were found in LaB_6. Taking into account that the ionic radius of yttrium $r_i(Y^{3+}) \sim 1.04$ Å is significantly lower than that of La^{3+} ($r_i \sim 1.17$ Å), which points to loosely bound states of Y^{3+} ions in the boron sublattice, a strong nonequilibrium state with a considerable structural disorder together with formation of TLSs having a low barrier height can be expected for YB_6. Moreover, the observed ratio B/Y (about 6.1 [9]) in the YB_6, which is large compared to the stoichiometric value for hexaborides, suggest the presence of a large number of vacancies in the sublattice of yttrium which prevails the vacancy concentration on B_6 sites.

The above estimated barrier height of the double-well potential TLS_2 $\Delta E_2 \approx 50$ K (Table IV) should be therefore related to the glass transition temperature $T^* \sim 50$ K which corresponds to the occurrence of structural disorder in the subsystem of Y^{3+} ions in YB_6. Detailed measurements of sample No. 1 were undertaken to investigate the heat capacity of YB_6 in the vicinity of the phase transition. With the aim to identify the anomaly at T^* one needs to compensate the strong quasilinear $C(T)$ decrease observed above 60 K to demonstrate the feature at $T^* \sim 50$ K. When describing the experimental $C(T)$ curve by a linear approximation $C(T) = AT + B$ found in the range 65–100 K (Fig. 3) the anomaly at $T^* \approx 55$ K becomes clearly discerned slightly above the steplike Einstein-type component [see inset in Fig. 3(a)]. At the same time also features found in the vicinity of $T^* \sim 50$ K on the temperature dependences of Hall coefficient $R_H(T)$ (Fig. 10) and on Seebeck coefficient $S(T)$ (Fig. 11) should be considered as anomalies that arise near this phase transition. Among features detected in YB_6 just below $T^* \sim 50$ K the authors of Ref. [3] point to a dramatic decrease of the linear thermal expansivity, and a significant amplitude lowering of the low-frequency Raman peak at 70 cm^{-1} was observed in the temperature range 30–60 K in Ref. [52]. It is worth noting that unlike to cage glasses LuB_{12} and LaB_6 in which high charge carrier motilities $\mu_H \sim 2500$ $cm^2/(V\,s)$ [90] and ~21 000 $cm^2/(V\,s)$ [91] were observed, respectively, in YB_6 the proximity to lattice instability and the resultant stronger structural disorder cause a dramatic suppression of Hall mobility. In the samples No. 1, No. 2, No. 3, and No. 4 with different concentrations of boron vacancies n_v and of paramagnetic centers $N_1 = N_{m0}$ (see Tables IV and V) the low-temperature mobility values are small enough and they do not exceed 50 $cm^2/(V\,s)$ (insets in Fig. 10). Moreover, in sample No. 4 the mobility at liquid helium temperature reaches only a value of 20 $cm^2/(V\,s)$ [inset in Fig. 10(c)]. These mobility values correspond to a very small value of the relaxation time $\tau_e = 1.3$–2.8×10^{-14} s and of the mean free path of the charge carriers $l = 11$–58 Å (Table III). Additionally, the close to square root power-law dependence $\mu_H \sim T^{-\alpha}$ ($\alpha \sim 0.5$) of the mobility in YB_6 (see insets in

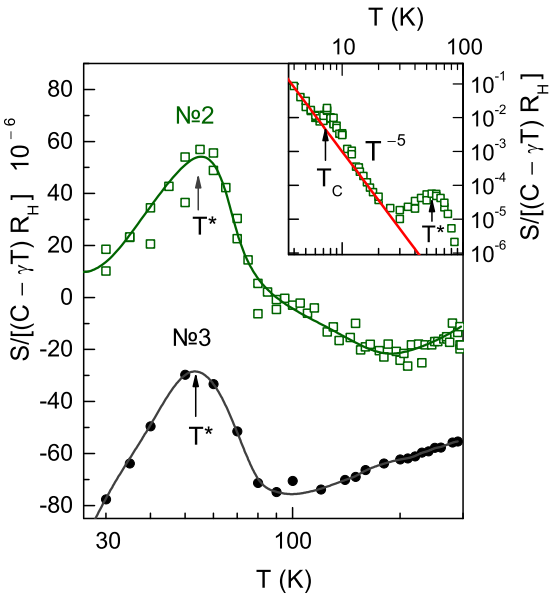

FIG. 17. Temperature dependences of the parameter $S/[(C - \gamma T)R_H]$ for samples No. 2 and No. 3 of YB_6. The inset shows the approximation of data by exponential dependence $\sim T^{-5}$ (see text). Arrows indicate the superconducting transition (T_c) and the cage-glass transition (T^*) temperatures.

Fig. 10) is significantly weaker than those observed in LuB_{12} ($\alpha \sim 2.06$) [90] and LaB_6 ($\alpha \sim 3$) [91]. It is also worth noting that substantial structural distortions in YB_6 were detected by low-temperature Raman studies [52].

To analyze the features of charge transport and of thermodynamic characteristics near T^* the relation

$$S_{\text{ph}} = (C_{\text{ph}}/ne)[1 + \tau_{\text{e-ph}}/\tau]^{-1}, \tag{18}$$

which connects the Hall coefficient $R_H = -1/ne$, the phonon drag thermopower S_{ph}, and the phonon contribution to the heat capacity C_{ph} [92], was used [in relation (18) $\tau_{\text{e-ph}}$ and τ denote the electron-phonon relaxation time and the relaxation time of the phonon gas, respectively]. Using the experimental results of Figs. 3, 10, and 11 it is then possible to obtain an estimation of the temperature dependence of the factor $[1 + \tau_{\text{e-ph}}/\tau]^{-1} = S/[(C - \gamma T)R_H]$, which determines the relative change of relaxation times in the system of conduction electrons. It can be seen in Fig. 17 that the parameter $[1 + \tau_{\text{e-ph}}/\tau]^{-1}$ of YB_6 samples passes through a maximum in the vicinity of $T^* \sim 50$ K and that the cage-glass transition temperature T^* corresponds to a sharp change in charge carriers scattering. In the cage-glass phase at temperatures below 20 K, where charge carriers scattering by impurities and structural defects becomes dominant ($\rho_0 \approx const$ and $\tau_{\text{e-ph}} \approx const$, see Fig. 2 and insets in Fig. 10), we observed a strong power-law dependence of $[1 + \tau_{\text{e-ph}}/\tau]^{-1} \sim T^{-5}$ which should correspond to the scattering in the phonon subsystem [93]. A detailed quantitative analysis of the charge transport anomalies requires a correct separation of two contributions to Seebeck coefficient—the negative (Mott-type) diffusion thermopower and the phonon drag effect on the Einstein modes—which is beyond the scope of this paper and will be published elsewhere. At the same time, the temperature dependence of $[1 + \tau_{\text{e-ph}}/\tau]^{-1} = S/[(C - \gamma T)R_H]$ (Fig. 17) allows us to confirm that in YB_6 there are two phase transitions—at $T^* \sim 50$ K and at $T_c \sim 4.2$–7.6 K—into the cage-glass state and into the superconducting state, correspondingly.

4. Factors responsible for the T_c dispersion

To quantify the offset from the stoichiometric composition state in YB_6 one can use parameters N_E and N_2 which were found from the heat capacity analysis shown in Fig. 15 by Eqs. (15) and (16) and determine the number of vacancies in Y and B sublattices, respectively. The concentration of vacancies of yttrium $n_v(\text{Y}) = 1 - N_E \approx 3$–5.5% and boron $n_v(\text{B}) = N_2/4 \approx 0.25$–1.1% of samples under investigation are given in Table IV. The resulting chemical composition (see Table IV) is then $\sim Y_{0.95}B_{5.94}$ (for samples No. 1 and No. 2), $Y_{0.96}B_{5.95}$ (for sample No. 3), and $Y_{0.97}B_{5.98}$ (for sample No. 4) and provides a Y/B ratio in the range of 6.15–6.25. This ratio is in agreement with the abovementioned results of Ref. [9] and allows us to link the variations of T_c with significant deviations from the hexaboride stoichiometry both in the yttrium and boron subsystem. Thus, taking into account the x-ray density $g_m = 3.705$ g/cm^3, which within experimental accuracy remains equal for all investigated YB_6 crystals, one can estimate from the heat capacity analysis made above (see Fig. 15) the mass density values $g_m^C = 3.57$–3.64 g/cm^3 of samples No. 1–4 (see Table IV and Fig. 14) by the relation

$$g_m^C = \frac{([1 - n_v(\text{Y})]m_{\text{Y}} + 6[1 - n_v(\text{B})]m_{\text{B}})1.66057 \times 10^{-24}}{a_0^3 \times 10^{-24}}, \tag{19}$$

where a_0 is the lattice parameter, and m_{Y} and m_{B} denote the atomic mass of yttrium and boron, correspondingly. Results of independent hydrostatic density measurements of No. 1–No. 3 crystals are also shown in Table IV and in Fig. 14. As can be seen from Table IV and Fig. 14, the parameters g_m^C and g_m are in good agreement with each other, and, as expected, the lower density observed for samples No. 1 and No. 2 meets the higher concentration of vacancies on yttrium and boron sites.

From these results a direct correlation between the development of the structural instability in YB_6 crystals and their transition temperature T_c can be seen. Namely, the nonequilibrium state is stabilized in crystals No. 1 and No. 2 by a higher concentration of vacancies in yttrium and boron sublattices, corresponding to higher transition temperature values $T_c = 7.4$–7.55 K. On the other side, the lower transition temperature values $T_c = 6.6$ K and 4.2 K observed in samples No. 3 and No. 4, respectively, correspond to a lower concentration of Y and B vacancies in these more stoichiometric YB_6 crystals. Taking into account that the YB_6 lattice is stabilized in the inhomogeneity range by introducing structural defects (vacancies), the near stoichiometric crystals No. 3 and No. 4 are more unstable, they are nonequilibrium ones. Moreover, in samples No. 3 and No. 4 there is an additional superconductivity suppression mechanism associated with Cooper pairs breaking by scattering on localized magnetic moments of vacancy complexes, but this factor is not the decisive one. When comparing the superconducting characteristics of YB_6 samples (Tables I and II), we can note that crystals No. 3 and No. 4 with the highest paramagnetic

response have the smallest T_c and H_{cm} values, but the upper critical field $H_{c2}(0)$ and the derivative $dH_{c2}/dT(T_c)$ of these two samples are the highest. Samples No. 3 and No. 4 exhibit also the highest values of Ginzburg-Landau-Maki parameters κ_1 and κ_2 [Fig. 13], together with the lowest amplitude of the ΔC jump near T_c (Table I and Fig. 14) and a significant broadening of the heat capacity anomaly (Fig. 4).

Considering a significant softening of the low-frequency phonon modes with temperature lowering in YB_6 found in Ref. [94], we may expect a relation between the softening and the enhancement of electron-phonon interaction, leading to a T_c increase in samples No. 1 and No. 2. Authors of Ref. [94] pointed out that just above the transition to superconducting state the low-frequency branches in Raman spectra exhibit energies of ~42 cm^{-1} (~5 meV) and ~60–70 cm^{-1} (~8 meV). Similarly, when creating the Eliashberg function $\alpha^2(\omega)F(\omega)$ from tunneling spectra measured on YB_6 single crystals with $T_c \approx 7.1$ K, two features were found on $\alpha^2(\omega)F(\omega)$ in Ref. [35]—a "shoulder" at 4.9 meV and a broad peak in the vicinity of 8.5 meV. In addition, authors of Ref. [35] estimated the electron-phonon interaction constant $\lambda_{e\text{-}ph} \approx 0.9$. Similar values of the energy of Einstein oscillators $\Theta_{E1} \approx 51$ K (~4.5 meV) and $\Theta_{E2} \approx 90$ K (~8 meV) in YB_6 were obtained from the analysis of phonon heat capacity in Ref. [3]. Taking into account the results of the present study, it seems to be reasonable that the above features observed experimentally at ~50 K should be associated with the barrier value of the double-well potential ΔE_2 (Table IV) which corresponds to the cage-glass transition temperature $T^* \approx \Delta E_2/k_B \approx 50$ K. Moreover, the barrier $\Delta E_2/k_B \approx 50$ K may be associated with a pseudogap in the YB_6 superconductor. Note that the barrier $\Delta E_2/k_B \approx 90$ K found in Refs. [48] and [49] for LaB_6 correlates very well with the pseudogap value $\Delta/k_B \leqslant 100$ K detected in Ref. [87] for this hexaboride. Thus, in accordance with the conclusions of Refs. [3] and [35], the formation of Cooper pairs in YB_6 crystals with the highest T_c occurs through the electron-phonon interaction with quasilocal vibrations of yttrium ions with energies $\Theta_E \approx 8$ meV. Using parameters $\langle\omega_{ln}\rangle \approx \Theta_E \approx 97.2$ K, $\lambda_{e\text{-}ph} \approx 0.96$ obtained in this work in the strong coupling limit and taking the Coulomb pseudopotential $\mu^* \sim 0.07$, within the framework of the relation for superconducting transition temperature [95]

$$k_B T_c = \frac{\hbar\langle\omega_{ln}\rangle}{1.2}\exp\left[-\frac{1.04(1+\lambda_{e\text{-}ph})}{\lambda_{e\text{-}ph}-\mu^*(1+0.62\lambda_{e\text{-}ph})}\right], \quad (20)$$

we obtain $T_c \approx 7.3$ K, which correlates very well with $T_c = 7.4$–7.55 K observed for crystals No. 1 and No. 2 of YB_6. Taking into account the only small variation of the concentration of conduction electrons (Fig. 10) one may expect only minor changes of the Coulomb pseudopotential $\mu^* \sim 0.07$ in YB_6 superconductors. Then, knowing μ^* and $\lambda_{e\text{-}ph}$ for crystals No. 1–No. 4 [Fig. 14] it is useful to compare the ratio $T_c/\langle\omega_{log}\rangle = f(\lambda_{e\text{-}ph})$ estimated for these samples from Eq. (20) with the universal ones describing the well-known experiments and calculations for strong coupling superconductors with $\lambda_{e\text{-}ph} < 1.5$ [95]. Figure 18 shows a good agreement in the $T_c/\langle\omega_{log}\rangle$ vs $\lambda_{e\text{-}ph}$ scaling of Pb-Tl-Bi, In-Tl, Sn, Hg, Ga, V, Nb, Mo, W, and Nb_3Sn data from Ref. [95] with these of YB_6 crystals No. 1 and No. 2 together with the approximation

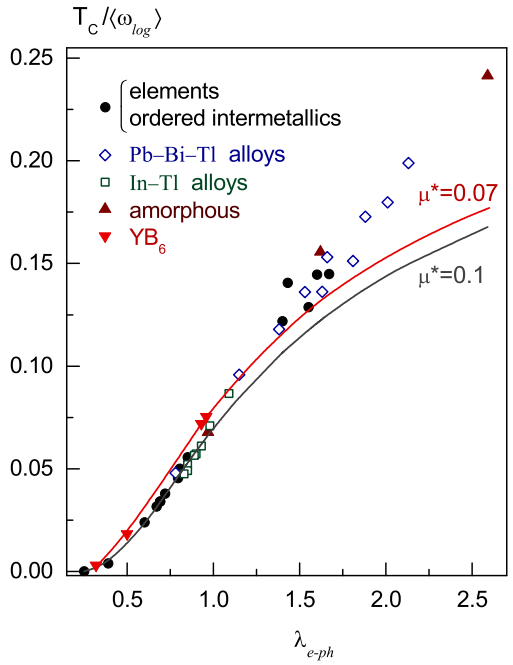

FIG. 18. The universal $T_c/\langle\omega_{log}\rangle$ vs $\lambda_{e\text{-}ph}$ scaling demonstrates the well-known experiments and calculations for strong coupling superconductors with $\lambda_{e\text{-}ph} < 1.5$ (Pb-Tl-Bi, In-Tl, Sn, Hg, Ga, V, Nb, Mo, W, and Nb_3Sn, see Ref. [95] for details) together with the results of this study for YB_6 crystals. The approximation by Eq. (20) is shown for $\mu^* \sim 0.07$ and $\mu^* \sim 0.1$.

of samples No. 1–No. 4 by Eq. (20) using both $\mu^* \sim 0.07$ and $\mu^* \sim 0.1$. This scaling supports the conclusion about superconductivity in the regime of strong coupling in YB_6 and allows us to estimate roughly the parameter $\langle\omega_{log}\rangle \sim 1500$ K $\sim \Theta_D \approx 1160$ K for crystal No. 4. Certainly, the huge increase of $\langle\omega_{log}\rangle$ from ~100 K (crystals No. 1 and No. 2) to ~1500 K in crystal No. 4 argues in favor of the development of a strong lattice instability in more stoichiometric yttrium hexaboride. Indeed, both the resistivity and the heat capacity temperature dependences demonstrate a strong renormalization of the electron-phonon interaction between samples No. 1 and No. 2, on one side, and No. 4, on the other side, together with a shift of anomalies of both the resistivity derivative $d\rho/dT$ and the heat capacity along the T axis to higher temperatures [see Figs. 16(a) and 16(b), correspondingly]. It can be seen from Fig. 14 that the depression of superconductivity is accompanied by an increase of mass density and a decrease of deviation from stoichiometry in YB_6 crystals demonstrating that vacancies both in boron and yttrium sites serve as a stabilizing factor in the nonequilibrium hexaboride lattice with enhanced electron-phonon interaction.

5. *Residual resistivity in* YB_6

To explain the lower values of residual resistivity ρ_0 in samples No. 1 and No. 2 where higher T_c values were observed (Fig. 2) in combination with higher concentrations of boron and yttrium vacancies (Table IV), the stabilizing effect of vacancies on the nonequilibrium crystal structure of YB_6 may be considered. Within this approach, more stoichiometric compositions appeared in crystals No. 3 and No. 4 are characterized

by a development of *bcc* lattice instability which leads to strong lattice distortion and disordering effects, reinforcing the charge carrier scattering on structural defects and their complexes and, as a result, to a higher residual resistivity. Indeed, vacancy complexes can be namely considered as nonpoint defects which provide significant structural distortions and are also related to magnetic moments of ~2.8–4.3 μ_B (see Table V). Structural distortions near these clusters of defects, along with a ρ_0 increase, lead also to an increase of heat capacity and to broadening of $C(T)$ features' at T_c seen in crystals No. 3 and No. 4 (Fig. 4).

V. CONCLUSIONS

A correlation of experimental results obtained from resistivity, Hall and Seebeck coefficients, heat capacity, magnetization, and hydrostatic density measurements of YB_6 allowed us to assume the transition into an unusual cage-glass state at $T^* \sim 50$ K in which the yttrium ions are displaced from their central positions in boron B_{24} cubooctahedra and located randomly in these cavities of the rigid covalent boron sublattice. We have shown that the number of vacancies on boron (0.25–1.1%) and yttrium (3–5.5%) sites may be considered as a measure of this nonequilibrium state in YB_6. The increase of vacancy concentration serves as a stabilizing factor of the YB_6 lattice leading to an enhancement of the electron-phonon interaction and to a T_c increase in this superconductor. On the other hand, the lowering of T_c in the cage-glass structure of YB_6 may be attributed to the development of a structural instability in the vicinity of stoichiometric composition. This instability evokes a hexaboride lattice distortion, disordering and accumulation of nonpoint defects into large complexes and a pair-breaking effect caused by the nonequilibrium state formation.

Moreover, from comprehensive and detailed studies of the superconducting and normal state properties we have determined a set of parameters including the electron-phonon interaction constant $\lambda_{\text{e-ph}} = 0.32$–$0.96$, the critical ($H_{c1}$ and H_{c2}) and thermodynamic (H_{cm}) magnetic fields, the coherence length $\xi(0) \sim 320$–340 Å, the penetration depth $\lambda(0) \sim 1100$–3250 Å and the mean free path $l = 11$–58 Å, the Ginzburg-Landau-Maki parameters $\kappa_{1,2}(0) \sim 3.3$–9.5, the superconducting gap $\Delta(0) \sim 6.2$–14.8 K, and the ratio $2\Delta(0)/k_B T_c \sim 3$–$4$. This set of parameters points in favor of type II superconductivity in the "dirty limit" $\xi \gg l$ with a medium to strong electron-phonon interaction and s-type pairing of the charge carriers in the nonequilibrium yttrium hexaboride.

ACKNOWLEDGMENTS

We would like to thank G. E. Grechnev, P. Samuely, and V. Moshchalkov for helpful discussions. The study was supported by RFBR Projects No. 15-02-02553a and 16-02-00171a. The measurements were partially carried out in the Shared Facility Centre of the P. N. Lebedev Physical Institute of RAS. K.F. and S.G. acknowledge partial support by Slovak agencies VEGA (2/0032/16) and APVV (14-0605).

[1] J. Nagamatsu, N. Nakagawa, T. Muranaka, Y. Zenitani, and J. Akimitsu, Nature (London) **410**, 63 (2001).
[2] N. E. Sluchanko, A. N. Azarevich, A. V. Bogach, I. I. Vlasov, V. V. Glushkov, S. V. Demishev, A. A. Maksimov, I. I. Tartakovskii, E. V. Filatov, K. Flachbart, S. Gabáni, V. B. Filippov, N. Yu. Shitsevalova, and V. V. Moshchalkov, JETP **113**, 468 (2011); N. E. Sluchanko, A. N. Azarevich, S. Yu. Gavrilkin, V. V. Glushkov, S. V. Demishev, N. Yu. Shitsevalova, and V. B. Filippov, JETP Lett. **98**, 578 (2013).
[3] R. Lortz, Y. Wang, U. Tutsch, S. Abe, C. Meingast, P. Popovich, W. Knafo, N. Shitsevalova, Y. B. Paderno, and A. Junod, Phys. Rev. B **73**, 024512 (2006).
[4] Z. Fisk, P. H. Schmidt, and L. D. Longinotti, Mater. Res. Bull. **11**, 1019 (1976).
[5] S. Kunii, T. Kasuya, K. Kadowaki, M. Date, and S. B. Woods, Solid State Commun. **52**, 659 (1984).
[6] S. Gabáni, I. Takáčová, G. Pristáš, E. Gažo, K. Flachbart, T. Mori, D. Braithwaite, M. Mášek, K. V. Kamenev, M. Hanfland, and P. Samuely, Phys. Rev. B **90**, 045136 (2014).
[7] V. Gasparov, I. Sheikin, and Sh. Otani, Physics C **460–462**, 623 (2007).
[8] Z. Fisk, A. C. Lawson, and R. W. Fitzgerald, Mater. Res. Bull. **9**, 633 (1974).
[9] S. Otani, M. M. Korsukova, T. Mitsuhashi, and N. Kieda, J. Cryst. Growth **217**, 378 (2000).
[10] K. E. Spear, in *Refractory Materials, Phase Diagrams*, edited by A. M. Alper (Academic Press, New York, 1976), Vol. 4, pp. 91/159.
[11] W. B. Pearson, *The Crystal Chemistry and Physics of Metals and Alloys*, Wiley Series on the Science and Technology of Materials (John Wiley & Sons, Inc., New York-London-Sydney-Toronto, 1972), p. 806.
[12] P. K. Liao and K. E. Spear, J. Phase Equilib. **16**, 521 (1995).
[13] T. Kasuya, J. Magn. Magn. Mater. **174**, L28 (1997).
[14] B. G. Lazarev, A. I. Sudovtsov, and E. E. Smirnov, Sov. Phys. JETP **6**, 816 (1958).
[15] M. Okamoto, K. Takei, and Y. Maeda, Jpn. J. Appl. Phys. **26**, 1323 (1987); **26**, 386 (1987).
[16] W. Buckel and W. Gey, Z. Phys. **176**, 336 (1963).
[17] J. Chevrier, J. B. Suck, J. C. Lasjaunias, M. Perroux, and J. J. Capponi, Phys. Rev. B **49**, 961 (1994).
[18] N. E. Sluchanko, V. V. Glushkov, S. V. Demishev, N. A. Samarin, A. K. Savchenko, J. Singleton, W. Hayes, V. V. Brazhkin, A. A. Gippius, and A. I. Shulgin, Phys. Rev. B **51**, 1112 (1995).
[19] A. A. Gippius, N. E. Sluchanko, V. V. Glushkov, S. V. Demishev, M. V. Kondrin, A. A. Pronin, V. V. Brazhkin, V. V. Moshchalkov, and Y. Bruynseraede, J. Phys.: Condens. Matter **12**, 9167 (2000).
[20] N. E. Sluchanko, V. V. Glushkov, S. V. Demishev, M. V. Kondrin, T. V. Ischenko, W. Gust, V. V. Brazhkin, B. B. Straumal, Y. Bruynseraede, and V. V. Moshchalkov, Phys. Rev. B **61**, 6019 (2000).
[21] V. N. Trofimov, Cryogenics **32**, 513 (1992).
[22] N. E. Sluchanko, A. V. Bogach, V. V. Glushkov, S. V. Demishev, M. I. Ignatov, N. A. Samarin, G. S. Burkhanov, and O. D. Chistyakov, JETP **98**, 793 (2004).

[23] N. E. Sluchanko, V. V. Glushkov, S. V. Demishev, M. V. Kondrin, N. A. Samarin, V. V. Moshchalkov, and V. V. Brazhkin, JETP **86**, 190 (1998).

[24] H. A. Bowman, R. M. Schoonover, and M. W. Jones, J. Research Nat. Bur. Stand.-C Engin. Instrum. C **71**, 179 (1967).

[25] C. S. Lue, J. H. Ross, Jr., C. F. Chang, and H. D. Yang, Phys. Rev. B **60**, R13941(R) (1999).

[26] B. R. Coles, Physica B **223–224**, 260 (1996).

[27] K. A. Gschneidner, Jr., J. Tang, S. K. Dhar, and A. Goldman, Physica B **163**, 507 (1990).

[28] See Supplemental Material at http://link.aps.org/supplemental/10.1103/PhysRevB.96.144501 for more information. (Heat capacity dependences of sample No. 3 at temperatures 0.4–10 K in external magnetic field $H \leqslant 60$ kOe. (a) The black linear γT dependence corresponds to the Sommerfeld term with $\gamma \approx 2.94\,\mathrm{mJ/(mol\,K^2)}$. The red solid line shows the experimental curve approximation by sum $\gamma T + C_D + C_E + C_{\mathrm{Sh}_2}$ [see text and Eqs. (14)–(16) for details]. Panel (b) shows the magnetic component $C_m = C - \gamma T - C_D - C_E - C_{\mathrm{Sh}_2}$ of sample No. 3 and the fitting of C_m by two additive terms. TLS_1 (dash-dot line) and TLS_m indicate the Shottky components C_{Sh_1} and C_{Sh_m}, correspondingly [see Eq. (16)]. Panels (c) and (d) summarize the characteristics of TLS_m component, the concentration of magnetic centers N_m, and Zeeman splitting ΔE_m in magnetic field. The solid line in panel (d) corresponds to g factor $\mathrm{g} = 0.51 \pm 0.02$ (Fig. S1); the Seebeck coefficient $S(T)$ is described by the sum $S_{\mathrm{ph}}(T) + S_0$, where $S_{\mathrm{ph}}(T) = S^0_{\mathrm{ph}}(\Theta_E/T)^2 \exp(\Theta_E/T)[\exp(\Theta_E/T) - 1]^{-2}$ is a phonon-drag thermopower with single Einstein mode and S_0 a vertical shift (Fig. S2); scaling of the results obtained from magnetic measurements: (a) the normalized ratio of thermodynamic $H_{\mathrm{cm}}/H_{\mathrm{cm}}(0)$ and (b) the upper critical $H_{c2}/H_{c2}(0)$ fields plotted as a function of reduced temperature for various samples (Fig. S3).)

[29] V. L. Ginzburg, Usp. Fiz. Nauk **161**, 1 (1991) [Sov. Phys. Usp. **34**, 101 (1991)].

[30] N. R. Werthamer, E. Helfand, and P. C. Hohenberg, Phys. Rev. **147**, 295 (1966).

[31] B. Jäger, S. Paluch, W. Wolf, P. Herzig, O. J. Żogał, N. Shitsevalova, and Yu. Paderno, J. Alloys Compd. **383**, 232 (2004).

[32] G. E. Grechnev, A. E. Baranovskiy, V. D. Fil, T. V. Ignatova, I. G. Kolobov, A. V. Logosha, N. Yu. Shitsevalova, V. B. Filippov, and O. Eriksson, Low Temp. Phys. **34**, 1167 (2008).

[33] K. Maki, Phys. Rev. **148**, 362 (1966).

[34] S. Szabo, J. Girovsky, Z. Pribulova, J. Kachmarchik, T. Mori, and P. Samuely, Supercond. Sci. Technol. **26**, 045019 (2013).

[35] R. Schneider, J. Geerk, and H. Reitschel, Europhys. Lett. **4**, 845 (1987).

[36] S. Souma, H. Komoda, Y. Iida, T. Sato, T. Takahashi, and S. Kunii, J. Electron Spectrosc. Relat. Phenom. **144–147**, 503 (2005).

[37] M. I. Tsindlekht, V. M. Genkin, G. I. Leviev, I. Felner, O. Yuli, I. Asulin, O. Millo, M. A. Belogolovskii, and N. Yu. Shitsevalova, Phys. Rev. B **78**, 024522 (2008).

[38] A. A. Abrikosov, *Fundamentals of the Theory of Metals* (North Holland, Amsterdam, 1988).

[39] G. Eilenberger, Phys. Rev. **153**, 584 (1967).

[40] D. Saint-Jaims, G. Sarma, and E. J. Thomas, *Type II Superconductivity* (Pergamon Press, Oxford, 1969).

[41] B. A. Kovenskaya, A. I. Kondrashov, E. M. Dudnik, and V. F. Kolotun, in *Refractory Compounds of Rare Earth Metals* (Springer, Berlin, 1979), p. 36.

[42] R. Kadono, S. Kuroiwa, J. Akimitsu, A. Koda, K. Ohishi, W. Higemoto, and S. Otani, Phys. Rev. B **76**, 094501 (2007).

[43] S. Kimura, T. Nanba, S. Kunii, and T. Kasuya, Phys. Rev. B **50**, 1406 (1994).

[44] T. McConville and B. Serin, Phys. Rev. **140**, A1169 (1965).

[45] H. Chi and J. P. Carbotte, Phys. Rev. B **49**, 6143 (1994).

[46] D. Mandrus, B. C. Sales, and R. Jin, Phys. Rev. B **64**, 012302 (2001).

[47] J. Stankiewicz, M. Evangelisti, and Z. Fisk, Phys. Rev. B **83**, 113108 (2011).

[48] M. A. Anisimov, V. V. Glushkov, A. V. Bogach, S. V. Demishev, N. A. Samarin, S. Yu. Gavrilkin, K. V. Mitsen, N. Yu. Shitsevalova, A. V. Levchenko, V. B. Filippov, S. Gabáni, K. Flachbart, and N. E. Sluchanko, JETP **116**, 760 (2013).

[49] M. Anisimov, A. Bogach, V. Glushkov, S. Demishev, N. Samarin, S. Gavrilkin, K. Mitsen, N. Shitsevalova, A. Levchenko, V. Filippov, S. Gabáni, K. Flachbart, and N. Sluchanko, Acta Phys. Pol. A **126**, 350 (2014).

[50] N. Sluchanko, S. Gavrilkin, K. Mitsen, A. Kuznetsov, I. Sannikov, V. Glushkov, S. Demishev, A. Azarevich, A. Bogach, A. Lyashenko, V. Filipov, J. Vanacken, G. Zhang, and V. Moshchalkov, J. Supercond. Novel Magn. **26**, 1663 (2013).

[51] G. Schell, H. Winter, H. Rietschel, and F. Gompf, Phys. Rev. B **25**, 1589 (1982).

[52] H. Bando, T. Hasegawa, N. Ogita, M. Udagawa, and F. Iga, J. Phys. Soc. Jpn. **80**, SA053 (2011).

[53] A. Czopnik, N. Shitsevalova, V. Pluzhnikov, A. Krivchikov, Yu. Paderno, and Y. Onuki, J. Phys.: Condens. Matter **17**, 5971 (2005).

[54] K. Takegahara and T. Kasuya, Solid State Commun. **53**, 21 (1985).

[55] M. M. Korsukova, T. Lundström, V. N. Gurin, and L.-E. Tergenius, Z. Kristallogr. **168**, 299 (1984).

[56] V. A. Trounov, A. L. Malyshev, D. Yu. Chernyshov, M. M. Korsukova, V. N. Gurin, L. A. Aslanov, and V. V. Chernyshev, J. Phys.: Condens. Matter **5**, 2479 (1993).

[57] M. K. Blomberg, M. J. Merisalo, M. M. Korsukova, and V. N. Gurin, J. Alloys Compd. **217**, 123 (1995).

[58] M. Korsukova, [*Proc. 11th Int. Symp. Boron, Borides, and Related Compounds*, Tsukuba (1993)] JJAP Series **10**, 15 (1994).

[59] D. A. Parshin, Phys. Solid State **36**, 991 (1994) [Fiz. Tverd. Tela (S. Peterburg) **36**, 1809 (1994)].

[60] B. B. Laird and H. R. Schober, Phys. Rev. Lett. **66**, 636 (1991).

[61] A. P. Sokolov, R. Calemczuk, B. Salce, A. Kisliuk, D. Quitmann, and E. Duval, Phys. Rev. Lett. **78**, 2405 (1997).

[62] W. Schirmacher, G. Diezemann, and C. Ganter, Phys. Rev. Lett. **81**, 136 (1998).

[63] W. Götze and M. R. Mayr, Phys. Rev. E **61**, 587 (2000).

[64] J. W. Kantelhardt, S. Russ, and A. Bunde, Phys. Rev. B **63**, 064302 (2001).

[65] W. Schirmacher, G. Ruocco, and T. Scopigno, Phys. Rev. Lett. **98**, 025501 (2007).

[66] H. Shintani and H. Tanaka, Nat. Mater. **7**, 870 (2008).

[67] W. M. Yang, H. S. Liu, X. J. Liu, G. X. Chen, C. C. Dun, Y. C. Zhao, Q. K. Man, C. T. Chang, B. L. Shen, A. Inoue, R. W. Li, and J. Z. Jiang, J. Appl. Phys. **116**, 123512 (2014).
[68] A. N. Vasiliev, T. N. Voloshok, A. V. Granato, D. M. Joncich, Y. P. Mitrofanov, and V. A. Khonik, Phys. Rev. B **80**, 172102 (2009).
[69] G. Carini, Jr., G. Carini, G. D'Angelo, E. Gilioli, and C. Vasi, Philos. Mag. **95**, 2596 (2015).
[70] L. Hou, W. M. Yang, H. S. Liu, J. Huo, Y. Jiao, and Q. Liu, J. Low Temp. Phys. **179**, 343 (2015).
[71] Y. Li, H. Y. Bai, W. H. Wang, and K. Samwer, Phys. Rev. B **74**, 052201 (2006).
[72] A. I. Chumakov and G. Monaco, J. Non-Cryst. Solids **407**, 126 (2015).
[73] A. I. Chumakov, G. Monaco, A. Fontana, A. Bosak, R. P. Hermann, D. Bessas, B. Wehinger, W. A. Crichton, M. Krisch, R. Rüffer, G. Baldi, G. Carini, Jr., G. Carini, G. D'Angelo, E. Gilioli, G. Tripodo, M. Zanatta, B. Winkler, V. Milman, K. Refson, M. T. Dove, N. Dubrovinskaia, L. Dubrovinsky, R. Keding, and Y. Z. Yue, Phys. Rev. Lett. **112**, 025502 (2014).
[74] A. S. Ahmad, X. Zhao, M. Xu, D. Zhang, J. Hu, H. J. Fecht, X. Wang, Q. Cao, and J. Z. Jiang, J. Low Temp. Phys. **186**, 172 (2017).
[75] R. Monnier and B. Delley, Phys. Rev. Lett. **87**, 157204 (2001).
[76] X. F. Zhou, A. R. Oganov, Zh. Wang, I. A. Popov, A. I. Boldyrev, and H. T. Wang, Phys. Rev. B **93**, 085406 (2016).
[77] N. E. Sluchanko, A. N. Azarevich, M. A. Anisimov, A. V. Bogach, S. Y. Gavrilkin, M. I. Gilmanov, V. V. Glushkov, S. V. Demishev, A. L. Khoroshilov, A. V. Dukhnenko, K. V. Mitsen, N. Y. Shitsevalova, V. B. Filippov, V. V. Voronov, and K. Flachbart, Phys. Rev. B **93**, 085130 (2016).
[78] D. P. Young, D. Hall, M. E. Torelli, Z. Fisk, J. L. Sarrao, J. D. Thompson, H. R. Ott, S. B. Oseroff, R. G. Goodrich, and R. Zysler, Nature (London) **397**, 412 (1999).
[79] P. Vonlanthen, E. Felder, L. Degiorgi, H. R. Ott, D. P. Young, A. D. Bianchi, and Z. Fisk, Phys. Rev. B **62**, 10076 (2000).
[80] P. A. Alekseev, K. Flachbart, S. Gabáni, V. N. Lazukov, P. Priputen, M. Reiffers, J. Sebek, E. Santava, A. V. Dukhnenko, V. B. Filippov, and N. Yu. Shitsevalova, Phys. Solid State **52**, 914 (2010).
[81] M. A. Anisimov, A. V. Bogach, V. V. Glushkov, S. V. Demishev, N. A. Samarin, N. Yu. Shitsevalova, A. V. Levchenko, V. B. Filipov, A. V. Kuznetsov, and N. E. Sluchanko, Solid St. Phenom. **190**, 221 (2012).
[82] J. L. Gavilano, Sh. Mushkolaj, D. Rau, H. R. Ott, A. Bianchi, and Z. Fisk, Physica B **329–333**, 570 (2003).
[83] J. M. Tarascon, J. Etourneau, P. Dordor, P. Hagenmuller, M. Kasaya, and J. M. D. Coey, J. Appl. Phys. **51**, 574 (1980).
[84] D. J. Kim, J. Xia, and Z. Fisk, Nat. Mater. **13**, 466 (2014).
[85] N. E. Sluchanko, A. V. Azarevich, M. A. Anisimov, A. V. Bogach, S. Yu. Gavrilkin, V. V. Glushkov, S. V. Demishev, A. A. Maksimov, I. I. Tartakovskii, E. V. Filatov, V. B. Filippov, and A. B. Lyashchenko, JETP Lett. **103**, 674 (2016).
[86] N. Sluchanko, A. Bogach, N. Bolotina, V. Glushkov, S. Demishev, A. Dudka, V. Krassnorussky, O. Khrykina, K. Krasikov, V. Mironov, V. Filipov, and N. Shitsevalova, arXiv:1707.06516.
[87] V. R. R. Medicherla, S. Patil, R. Shankar Singh, and K. Maiti, Appl. Phys. Lett. **90**, 062507 (2007).
[88] Yu. S. Ponosov, and S. V. Strel'tsov, JETP Lett. **97**, 447 (2013).
[89] H. Werheit, V. Filipov, and N. Shitsevalova, Z. Anorg. Allg. Chem. **641**, 1835 (2015).
[90] N. Sluchanko, L. Bogomolov, V. Glushkov, S. Demishev, M. Ignatov, Eu. Khayrullin, N. Samarin, D. Sluchanko, A. Levchenko, N. Shitsevalova, and K. Flachbart, Phys. Status Solidi B **243**, 63(R) (2006).
[91] M. A. Anisimov, A. V. Bogach, V. V. Glushkov, S. V. Demishev, N. A. Samarin, N. Yu. Shitsevalova, and N. E. Sluchanko, Solid St. Phenom. **152–153**, 525 (2009).
[92] P. M. Chaikin, in *Organic Superconductivity*, edited by V. Z. Kresin and W. A. Little (Plenum Press, New York, 1990), p. 101.
[93] A. M. Kosevich, *Theory of Crystal Lattice* [Khar'kov State University, Vishcha Shkola, Khar'kov, 1988 (in Russian)], translated into English (WILEY-VCH, Berlin, New York, 1999).
[94] Yu. S. Ponosov, and N. Yu. Shitsevalova, JETP Lett. **102**, 295 (2015).
[95] P. Allen and R. Dynes, Phys. Rev. B **12**, 905 (1975).